J. Fluid Mech. (2006), *vol.* 564, *pp.* 25–55.
doi:10.1017/S0022112006001157 Printed in the United Kingdom

Nonlinear secondary flow through a rotating channel

By D. P. WALL AND M. NAGATA

Department of Aeronautics and Astronautics, Graduate School of Engineering, University of Kyoto, Kyoto, 606-8501 Japan

(Received 17 May 2004 and in revised form 6 February 2006)

The stability of fluid through a channel subject to a system rotation of constant rate about the spanwise axis is considered. In contrast to previous studies, a strongly nonlinear bifurcation approach is used to solve for a family of two-dimensional, steady, streamwise-orientated vortex flows. A stability analysis of these flows is also performed. All of the two-dimensional flows considered lose stability to an Eckhaus (streamwise-independent) secondary disturbance in a steady bifurcation to another member of the solution set. This property, given also that lower-order primary and secondary disturbance modes can become unstable, leads to a rich structure of bifurcation relationships between the secondary flows. With increasing Reynolds number, the secondary flow arising from the linear critical point first loses stability to the Eckhaus instability, and then loses stability to a fundamental spanwise mode with small streamwise wavenumber. With a further increase in Reynolds number, the secondary flow then also becomes unstable to a disturbance of subharmonic spanwise and $O(1)$ streamwise wavenumber, and finally (on the upper solution branch) a disturbance of fundamental spanwise and $O(1)$ streamwise wavenumber. Other types of bifurcation for possible tertiary flows are also identified. By superimposing the secondary disturbance onto the secondary flow, visualizations of the possible structure of the bifurcating tertiary flows are obtained. The visualizations show low-speed streaks in the streamwise velocity component lying between a set of staggered vortices for superharmonic bifurcations, and between aligned vortices for subharmonic bifurcations. Excellent qualitative and quantitative agreement is found with previous experimental results and direct-numerical-simulation-based stability studies, and good overall agreement with previous DNS studies was also found.

1. Introduction

Fluid flow subject to a system rotation about the spanwise axis can lose stability to an instability mechanism which produces longitudinal rolls. Tritton (1992) and Tritton & Davies (1985) describe this mechanism along with many examples of relevant rotating flows. A similar mechanism is also present for flows through curved geometry, and for flows with thermal stratification, as described by Guo & Finlay (1991) and Bradshaw (1969) respectively. The present problem thus has relevance to a large number of geophysical and astrophysical problems, including, for example, barotropic instabilities and flow through ocean trenches. More details of many of these problems may be found in Hopfinger & Linden (1990). We note that flow through a rotating channel is also relevant to many engineering problems where the effect of rotation on turbulent transition must be understood for the design of rotating

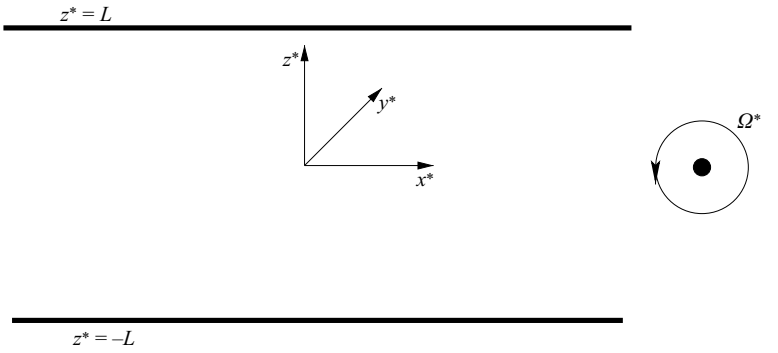

FIGURE 1. Configuration of the channel in dimensional coordinates.

machinery (for example compressor impellers or radial pump flows) or of instruments that measure mass flow rates based on the Coriolis effect, as described by Raszillier & Durst (1988) for example.

In the present study we shall consider channel flow subject to system rotation about an axis in the spanwise direction, y^*, as shown in figure 1. The stability of this flow is determined by two parameters: a rotation number and the Reynolds number, R. For non-zero values of the rotation number, the presence of the Coriolis force associated with the rotating reference frame produces a pressure gradient in the cross-channel z^*-direction in the basic flow. The linear stability of this flow was considered by Lezius & Johnstone (1976), who found a minimum critical Reynolds number, R_c^{ro}, of many orders of magnitude less than the corresponding value for plane Poiseuille flow. Experiments performed by Alfredsson & Persson (1989) showed the setting up of streamwise-orientated vortices when $R > R_c^{ro}$ and the rotation number lies in a certain range. The experimentally observed most unstable wavenumber of these disturbances was in agreement with that predicted by linear stability theory close to the linear critical point. This is in contrast with non-rotating plane Poiseuille flow, which first becomes unstable to transverse-orientated vortices according to linear stability theory, but which may also lose stability subcritically to other flows in noisy practical situations.

At higher values of R, as the rotation number is increased, a secondary instability occurs which leads to a three-dimensional travelling-wave type tertiary flow. Two instabilities of this type were identified in Alfredsson & Persson's (1989) study: an instability with streamwise wavelength of the order of the spanwise vortex wavelength, usually characterized by a twisting of the vortices, and an undulating instability with streamwise wavelength an order of magnitude larger than the spanwise wavelength. Alfredsson & Persson (1989) also observed another secondary instability consisting of the splitting and merging of the streamwise vortices. Finlay (1990) studied the two travelling-wave instabilities using a direct numerical simulation (DNS) approach, as well as performing a linear stability analysis of a numerically computed streamwise-vortex basic state to two-dimensional spanwise-independent modes. He found the undulating mode to exist only for low rotation rates, and to first appear for values of R between $1.3R_c^{ro}$ and $1.5R_c^{ro}$. The twisting mode was found to exist for a wide range of rotation rates, and first appeared for values of R between $2R_c^{ro}$ and $3R_c^{ro}$. Both Finlay (1990) and Yang & Kim (1991) found the twisting mode to have the largest growth rate, and so it would be expected to dominate in practice in flows where both modes existed. Matsubara & Alfredsson (1998) presented experimental results concerning the growth of the twisting-mode secondary instability, finding the

preferred most rapidly growing disturbance to be an out-of-phase, sinuous mode. Guo & Finlay (1991) considered an Eckhaus-type instability causing merging and splitting of vortices by performing a linear stability analysis of a DNS-generated two-dimensional vortex flow to two-dimensional streamwise-independent disturbance modes. They found this instability to be important in selecting the wavenumber of the streamwise vortices. Finlay's (1992) DNS study explored the later stages of transition to turbulence in these flows, while Kristoffersen & Andersson (1993) also performed DNS of the turbulent flow.

It may be noted that similar transitions to those of the present problem, composed of the loss of stability of the basic state to streamwise-orientated rolls, with the resultant secondary flow then losing stability to three-dimensional disturbances which are manifested as a modification on the streamwise structures, are also found in many other flows. Nagata (1986) considers a similar transition in Couette flow between two almost co-rotating cylinders, while DiPrima & Swinney (1985) identify a similar transition in Taylor–Couette flow, and Finlay, Keller & Ferziger (1988) describe a similar phenomenon in relation to flow through curved channels.

The aim of the present study is to find the two-dimensional secondary flow for rotating channel flow using a global bifurcation approach, which would allow the solution to be accurately computed away from the bifurcation point to large amplitude. (Note that in the present context, a two-dimensional secondary flow refers to a flow that is streamwise independent, and in particular does not refer to flows that are invariant in the direction of the axis of rotation (i.e. here spanwise independent) which are often referred to as two-dimensional in the context of rotating flows.) We also set out to examine the stability of these solutions so that we may know where they may be expected to exist, so that comparisons may be made with the previous experimental and DNS results described above. It should be noted that recently there has also been a developing interest in the relationship between unstable solutions and coherent structures observed in transitional and turbulent flows, see for example Waleffe (1998). These studies offer the possibility of deriving insight into the transition process which cannot be easily derived from DNS studies, as the latter can only describe stable solutions. The stability analysis also allows us to predict features of the tertiary flow, which may also be compared with DNS and experimental results.

Accordingly, in § 2 we formulate the problem in mathematical terms, solve the resultant equations for a basic flow and derive a corresponding set of primary disturbance equations. In § 3 we review the stability of the basic flow, including consideration of three-dimensional disturbances, and will use the analysis in the following section to construct the form of the bifurcating secondary flows. In § 4 we proceed to find a class of two-dimensional nonlinear secondary flows to which the basic flow first loses stability with increasing R. In § 5 we consider the stability of these secondary flows. In contrast to previous studies, we consider the stability of the present secondary flows to three-dimensional perturbations, and are able to identify a variety of different types of bifurcation to tertiary flows. In § 6 we compare results with those of the previous DNS and experimental studies, before summarizing our results in § 7.

2. Mathematical formulation

We adopt a Cartesian coordinate system whose origin is located on the centreline of the channel. The coordinates $x_1^* = x^*$, $x_2^* = y^*$ and $x_3^* = z^*$ represent the distances in the streamwise, transverse and wall-normal directions respectively, where an asterisk

denotes a dimensional variable. The following non-dimensional variables are adopted:

$$\boldsymbol{x} = \frac{\boldsymbol{x}^*}{L}, \quad \boldsymbol{u} = \frac{\boldsymbol{u}^*}{V}, \quad p = \frac{p^*}{\rho V^2}, \quad t = t^* \frac{V}{L}, \tag{1}$$

where L and ρ denote half the channel width and constant density respectively, and we select the velocity scale $V = \nu/L$, where ν denotes the constant kinematic viscosity. The variables u_i, p and t denote the component of velocity in the x_i-direction (we shall also use $\boldsymbol{u} = (u, v, w) = (u_1, u_2, u_3)$), pressure and time respectively. An illustration of the channel configuration is provided in figure 1. The flow through the channel is subject to a system rotation at a constant rate, Ω^*, about a spanwise-orientated axis as shown in the figure. With this choice of dimensions, restricting attention to incompressible flows, our problem is governed by the non-dimensional Navier–Stokes equations expressed in the rotating frame, together with the incompressibility condition given by

$$\frac{\partial u_i}{\partial t} + u_j \frac{\partial u_i}{\partial x_j} = -\frac{\partial p}{\partial x_i} + \frac{\partial^2 u_i}{\partial x_j \partial x_j} + \Omega(-u_3 \delta_{i,1} + u_1 \delta_{i,3}), \tag{2}$$

$$\frac{\partial u_j}{\partial x_j} = 0, \tag{3}$$

where $\Omega = 2(-\Omega^*)L^2/\nu > 0$ is a rotation number, and subject to the no-slip boundary conditions at the channel walls,

$$\boldsymbol{u}(z = \pm 1) = \boldsymbol{0}. \tag{4}$$

A basic-state solution of the form $\boldsymbol{u}(x, y, z, t) = u_0(z)\boldsymbol{i}$, $p(x, y, z, t) = p_0(x, z)$ is sought, where we define the unit vectors $\boldsymbol{i}$, $\boldsymbol{j}$ and $\boldsymbol{k}$ in the x-, y- and z- directions respectively. Substituting into equations (2) and (3) for a solution of this form, we obtain the basic flow

$$u_0(z) = R(1 - z^2), \tag{5}$$

where we have introduced the Reynolds number $R = L^3 J/2\rho\nu^2$, in which $-J$ $(J > 0)$ is the constant imposed pressure gradient along the channel in the positive x-direction. The basic-state velocity is thus of an identical parabolic form to that of the non-rotating plane Poiseuille flow case. However, in contrast to that case, for the present basic flow there is also a pressure gradient in the wall-normal direction,

$$\frac{\partial p_0}{\partial z} = R\Omega(1 - z^2).$$

We shall also make use of a second rotation number, $Rot = 4\Omega^* \rho\nu/JL$, when describing the linear stability results. For this case of laminar flow, the two rotation numbers are related by $Rot = \Omega/R$. We will also later compare results with Alfredsson & Persson (1989) who chose a rotation number, Ro^{AP}, and Reynolds number, Re^{AP} based on a flux-based velocity scale,

$$Rot^{AP} = \frac{2\Omega}{\int_{-1}^{1} u \, \mathrm{d}z}, \quad Re^{AP} = \int_{-1}^{1} u \, \mathrm{d}z.$$

In order to consider the stability of the basic flow, and also to permit the solution of the secondary flow which arises upon the basic flow's loss of stability, we seek a solution to the governing equations (2) and (3) subject to the boundary conditions

(4) in the form

$$\boldsymbol{u} = \boldsymbol{u}_0 + \hat{\boldsymbol{u}}, \quad p = p_0 + \hat{p},$$

and so we are left to solve

$$\frac{\partial \hat{\boldsymbol{u}}}{\partial t} + \boldsymbol{u}_0 \cdot \nabla \hat{\boldsymbol{u}} + \hat{\boldsymbol{u}} \cdot \nabla \boldsymbol{u}_0 + \hat{\boldsymbol{u}} \cdot \nabla \hat{\boldsymbol{u}} = -\nabla \hat{p} + \nabla^2 \hat{\boldsymbol{u}} + \Omega(-\hat{u}_3 \boldsymbol{i} + \hat{u}_1 \boldsymbol{k}), \tag{6}$$

$$\nabla \cdot \hat{\boldsymbol{u}} = 0, \tag{7}$$

subject to

$$\hat{\boldsymbol{u}}(z = \pm 1) = \boldsymbol{0}. \tag{8}$$

We decompose the velocity disturbance $\hat{\boldsymbol{u}}$ according to

$$\hat{\boldsymbol{u}} = \breve{U}(z, t)\boldsymbol{i} + \breve{\boldsymbol{u}}, \tag{9}$$

where the mean flow modification $\breve{U}(z, t)$ is the $x - y$ average of the component of $\hat{\boldsymbol{u}}$ in the x-direction. We may also exploit the solenoidal nature of the fluctuating part of the disturbance velocity, $\breve{\boldsymbol{u}}$, and further decompose this component into poloidal and toroidal parts so that the incompressibility condition (7) is automatically satisfied,

$$\breve{\boldsymbol{u}} = \nabla \times (\nabla \times (\phi \boldsymbol{k})) + \nabla \times \psi(\boldsymbol{k}). \tag{10}$$

Substituting expressions (9) and (10) into equation (6) for $\hat{\boldsymbol{u}}$ and applying the operators $\boldsymbol{k} \cdot \nabla \times (\nabla \times$ and $\boldsymbol{k} \cdot \nabla \times$, we obtain

$$\frac{\partial(\nabla^2 \Delta_2 \phi)}{\partial t} + U \nabla^2 \Delta_2 \phi_x - \frac{\partial^2 U}{\partial z^2} \Delta_2 \phi_x + \boldsymbol{k} \cdot \nabla \times (\nabla \times \breve{\boldsymbol{u}} \cdot \nabla \breve{\boldsymbol{u}}) = \nabla^4 \Delta_2 \phi - \Omega \Delta_2 \psi_y, \tag{11}$$

$$\frac{\partial(\Delta_2 \psi)}{\partial t} + U \Delta_2 \psi_x - \frac{\partial U}{\partial z} \Delta_2 \phi_y - \boldsymbol{k} \cdot \nabla \times \breve{\boldsymbol{u}} \cdot \nabla \breve{\boldsymbol{u}} = \nabla^2 \Delta_2 \psi + \Omega \Delta_2 \phi_y, \tag{12}$$

where Δ_2 is the two-dimensional Laplacian, $\Delta_2 = \partial^2/\partial x^2 + \partial^2/\partial y^2$, and $U = u_0(z) + \breve{U}(z, t)$ is the mean flow. An equation for the mean flow modification is obtained by taking the x–y average of the x-component of equation (6),

$$-\frac{\partial}{\partial z}(\overline{\Delta_2 \phi(\phi_{xz} + \psi_y)}) = \frac{\mathrm{d}^2 \breve{U}}{\mathrm{d}z^2}. \tag{13}$$

Equations (11), (12) and (13) are solved subject to the non-slip boundary conditions

$$\psi(\pm 1) = \phi(\pm 1) = \left.\frac{\partial \phi}{\partial z}\right|_{z=-1} = \left.\frac{\partial \phi}{\partial z}\right|_{z=1} = 0, \tag{14}$$

$$\breve{U}(z = \pm 1) = 0. \tag{15}$$

3. Linear stability

In this section we briefly describe the main features of the linear stability of rotating channel flow. In particular, in order to obtain the nonlinear secondary flows in the following section, we accurately determine the location of bifurcation points, and must understand the nature of the bifurcating flow. Neglecting terms involving products of the disturbance, and also the mean flow modification, $\breve{U}$, in equations (11) and (12), we consider three-dimensional disturbances in the normal temporal-mode form

$$\phi = \Phi(z) \mathrm{e}^{\mathrm{i}(\alpha x + \beta y) + \sigma t}, \tag{16}$$

$$\psi = \Psi(z) \mathrm{e}^{\mathrm{i}(\alpha x + \beta y) + \sigma t}, \tag{17}$$

where we assume the wavenumbers α and β are real and non-negative without loss of generality. We are left to solve a sixth-order linear differential system of the form

$$\frac{\mathrm{d}^4\Phi}{\mathrm{d}z^4} - [2(\alpha^2+\beta^2) + \mathrm{i}\alpha u_0]\frac{\mathrm{d}^2\Phi}{\mathrm{d}z^2} + \left[\mathrm{i}\alpha\left\{(\alpha^2+\beta^2)u_0 + \frac{\mathrm{d}^2u_0}{\mathrm{d}z^2}\right\} + (\alpha^2+\beta^2)^2\right]\Phi - \mathrm{i}\beta\Omega\Psi = \sigma\left[\frac{\mathrm{d}^2\Phi}{\mathrm{d}z^2} - (\alpha^2+\beta^2)\Phi\right], \quad (18)$$

$$\frac{\mathrm{d}^2\Psi}{\mathrm{d}z^2} - [(\alpha^2+\beta^2) + \mathrm{i}\alpha u_0]\Psi + \mathrm{i}\beta\left(\frac{\mathrm{d}u_0}{\mathrm{d}z} + \Omega\right)\Phi = \sigma\Psi, \quad (19)$$

subject to the boundary conditions

$$\Psi(z=\pm1) = \Phi(z=\pm1) = \frac{\mathrm{d}\Phi}{\mathrm{d}z}|_{(z=\pm1)} = 0. \quad (20)$$

Equations (18) and (19) subject to boundary conditions (20) together form a linear differential eigenvalue problem for σ as a function of α, β, R and Ω. We will denote the real and imaginary parts of the ith most unstable mode by σ_i^R and σ_i^I respectively. In order to obtain a numerical solution we expand the eigenfunctions Φ and Ψ in the Chebyschev series form

$$\Phi(z) = \sum_{k=0}^{\infty} a_k(1-z^2)^2T_k(z), \qquad \Psi(z) = \sum_{k=0}^{\infty} b_k(1-z^2)T_k(z), \quad (21)$$

where $T_k(z) = \cos(k\arccos(z))$ is the kth Chebyschev polynomial and the factors $(1-z^2)^2$ and $(1-z^2)$ ensure that the boundary conditions (20) are automatically satisfied. A Chebyschev collocation-point numerical technique is then applied by truncating the sums in expressions (21) at $k=N$, and evaluating equations (18) and (19) at the $N+1$ (internal) collocation points

$$z_i = \cos\frac{i\pi}{N+2}, \qquad i = 1, \ldots, N+1. \quad (22)$$

The resultant generalized algebraic eigenvalue problem for the coefficients a_k and b_k is solved using the QZ algorithm.

3.1. *Results*

Marginal stability curves ($\sigma_1^R = 0$) in the (R, Ω)- plane are plotted in figure 2 with instability occurring to the right of a given curve and stability to the left. According to our results, for a fixed value of Ω a two-dimensional mode (with $\alpha = 0$) first becomes unstable with increasing R. However, the value of the most unstable spanwise wavenumber, β, varies with R and Ω. For example in figure 2 it may be seen that for $\Omega > 100$ the basic flow loses stability to the ($\beta = 5$, $\alpha = 0$) mode before the ($\beta = 2.5$, $\alpha = 0$) mode as R increases, whereas this situation is reversed for $\Omega < 100$.

The linear stability results contained in the studies of Lezius & Johnstone (1976) and Alfredsson & Persson (1989) considered only two-dimensional ($\alpha = 0$) linear disturbances, since these correspond to the observed secondary flow. In figure 3 we have plotted the minimum critical Reynolds number, R_c as a function of α, together with the corresponding values of β, Rot, Ω and σ_1^I. It may be observed that the two-dimensional mode with $\alpha = 0$ indeed yields the smallest R_c. Lezius & Johnstone (1976) considered a sequence of discrete values of Rot and, in terms of the present dimensions, found the minimum critical Reynolds number to be $R_c = 66.40$ at

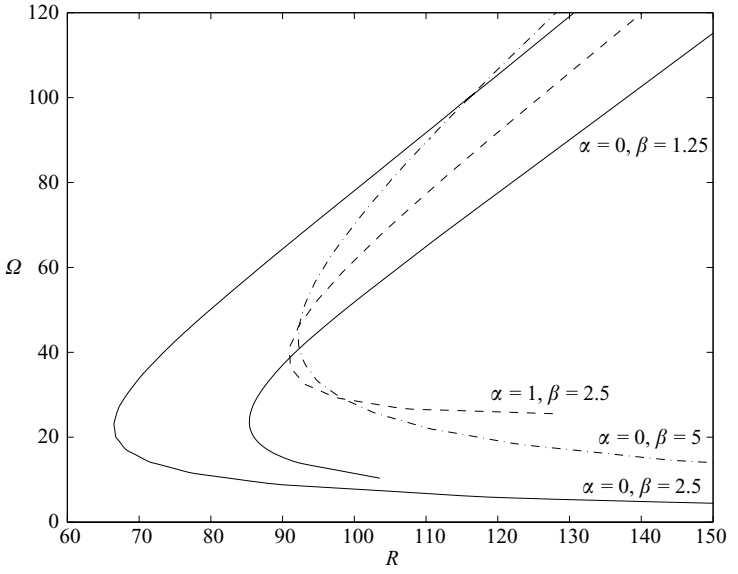

FIGURE 2. Marginal stability curves corresponding to the most unstable eigenvalue for the values of α and β indicated.

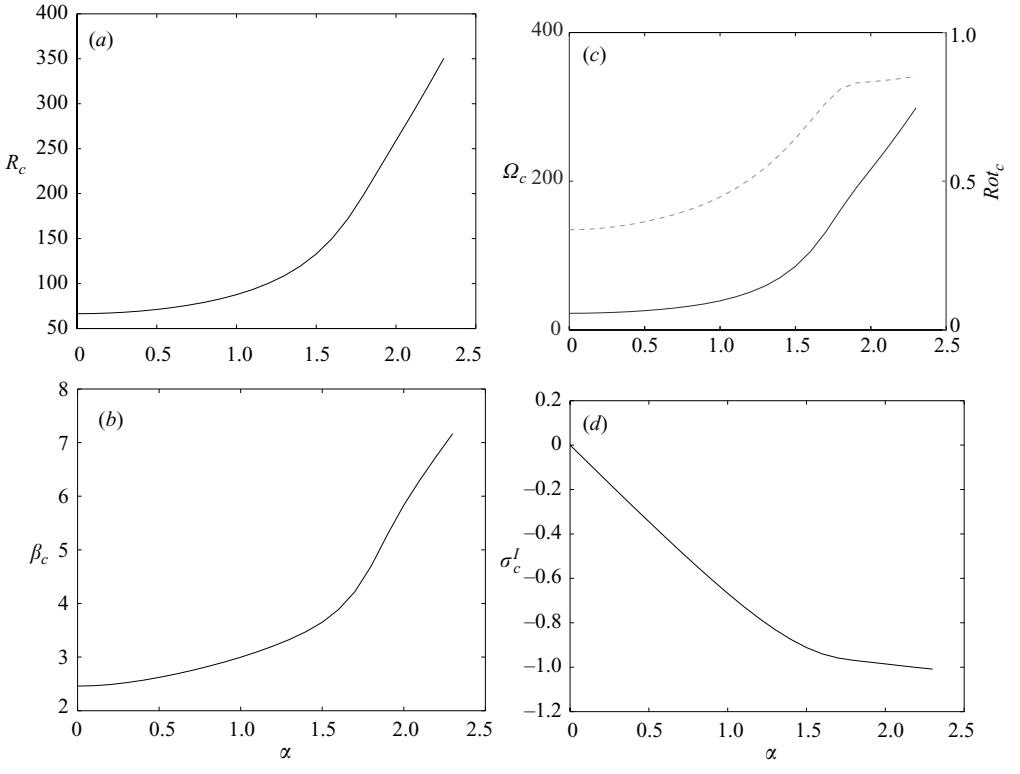

FIGURE 3. The linear critical point as a function of α: (*a*) $R_c(\alpha)$, (*b*) $\beta_c(\alpha)$, (*c*) - - -, $Rot_c(\alpha)$ and —, $\Omega_c(\alpha)$, and (*d*) $\sigma_c^I(\alpha)$.

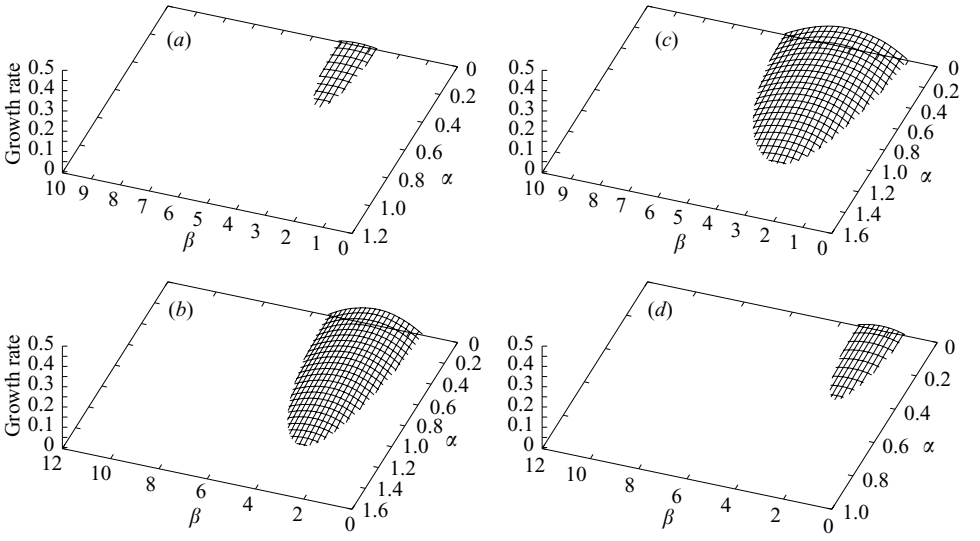

FIGURE 4. Growth rate of the most unstable mode against disturbance wavenumbers α and β at $R = 100$ for (*a*) $Rot = 0.8$, (*b*) $Rot = 0.6$, (*c*) $Rot = 0.35$, (*d*) $Rot = 0.1$. Only positive growth rates are plotted.

$Rot = 1/3$ with $\beta_c = 2.45$. Alfredsson & Persson (1989), who also considered a set of discrete values of Rot, found the minimum critical Reynolds number to be $R_c = 66.45$ also at $Rot = 1/3$. With the present numerical method, upon setting $Rot = 1/3$, we obtain a critical Reynolds number $R_c = 66.450$ with the corresponding $\beta_c = 2.455$. However, allowing Rot to vary, we obtain the minimum critical Reynolds number to be $R_c = 66.448$, $\beta_c = 2.459$ and $Rot_c = 0.3366$. For convenience however, most of our results in § 4 are for the near critical wavenumber $\beta = 2.5$, together with $\beta = 1.25$, $\beta = 3.75$ and $\beta = 5$ to facilitate an easier understanding of the one-two and one-three modal interactions described in those sections. It may also be observed from figure 3 that the corresponding critical spanwise wavenumber and both critical rotation numbers increase with α, while the critical eigenvalue is only real when $\alpha = 0$.

In figure 4 we have plotted values of $\sigma_R^1 > 0$ in the (α, β)- plane when $R = 100$ for four values of Rot. At this value of R the flow is stable to all infinitesimal disturbances when $Rot = 0$, and so clearly increases in Rot first destabilize the flow, with a region of unstable wavenumbers increasing in size, before further increases in Rot shrink this region and stabilize the flow. It may be observed that the largest growth rates occur when $\alpha = 0$, and so these two-dimensional modes may be expected to dominate.

For $R > 5772$ the flow is also unstable to a two-dimensional spanwise-independent shear mode as shown by figure 5. It may easily be seen that equations (18) and (19) are independent of Ω when $\beta = 0$, and so this mode is the well-known Tollmien–Schlichting mode that arises from consideration of the Orr–Sommerfeld equations for plane Poiseuille flow, as discussed by Drazin & Reid (1981) for example. As R increases further, the region of instability of the basic flow to this shear mode spreads to include non-zero β. However, for the values of Rot and R we investigated, the two regions of instability never intersect. Moreover, we note that the growth rate associated with the shear mode is several orders of magnitude smaller than that of the rotation modes, thus we would expect the latter to dominate in practice in a situation where both existed.

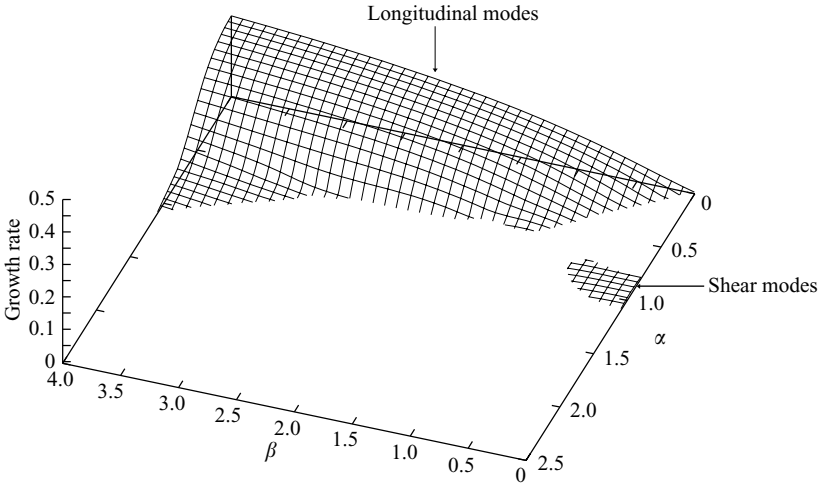

FIGURE 5. Plot of the growth rate of the most unstable mode for $R = 10^4$, $Rot = 0.1$. Only positive growth rates are plotted.

We also note the remark of Alfredsson & Persson (1989) that, in contrast to non-rotating Poiseuille flow, for the present problem lower-order eigenvalues may also become unstable. This enriches the range of possible bifurcating flows. For instance when $\Omega = 22.1325$ and $\beta = 2.5$ the next two eigenvalues, which are also real, become unstable at $R = 774$ and $R = 6811$ respectively.

In summary, we have found the basic flow to be most unstable to two-dimensional disturbances with $\alpha = 0$, with the corresponding eigenvalues real. The critical Reynolds number allowing Rot, α and β to vary is found to be $R_c = 66.448$.

4. Two-dimensional steady nonlinear secondary flows

4.1. *Numerical formulation*

The previous section describes how the basic flow is most unstable to two-dimensional disturbances. We seek to calculate the nonlinear secondary flows which bifurcate from the basic flow upon loss of stability to disturbances of this type. Accordingly we shall seek to calculate two-dimensional solutions to equations (11) and (12) with the nonlinear terms retained. (The nonlinear terms not explicitly expressed in these equations may be found in Wall & Nagata (2000).) Since the corresponding marginal eigenvalues are real, we anticipate a steady solution, and accordingly seek solutions in the form

$$\phi(y, z) = \sum_{l=0}^{\infty} \sum_{n=-\infty}^{\infty} a_{l,n} \mathrm{e}^{\mathrm{i}n\beta y} T_l(z)(1 - z^2)^2, \tag{23}$$

$$\psi(y, z) = \sum_{l=0}^{\infty} \sum_{n=-\infty}^{\infty} b_{l,n} \mathrm{e}^{\mathrm{i}n\beta y} T_l(z)(1 - z^2), \tag{24}$$

where the amplitude coefficients $a_{l,n}$ and $b_{l,n}$ are complex. Equations for the case $n = 0$ are replaced by the equation for the mean flow modification (13), where this

modification is decomposed according to

$$\check{U}(z) = \sum_{k=0}^{\infty} C_k T_k(z)(1 - z^2), \tag{25}$$

in which the coefficients C_k are real. Once again the $(1 - z^2)^2$ and $(1 - z^2)$ factors have been introduced to ensure that the boundary conditions (14) are automatically satisfied. Since ϕ and ψ are required to be real, we have that $\overline{\phi} = \phi$ and $\overline{\psi} = \psi$, where $\overline{Z}$ denotes the complex conjugate of Z, so we have

$$\sum_{l=0}^{\infty} \sum_{n=\infty}^{-\infty} \overline{a_{l,-n}} e^{in\beta y} T_l(z)(1 - z^2)^2 = \sum_{l=0}^{\infty} \sum_{n=-\infty}^{\infty} a_{l,n} e^{in\beta y} T_l(z)(1 - z^2)^2,$$

with a similar relationship holding for ψ. Thus we may truncate the sums in the expressions (23) and (24) to positive values of n, and calculate the coefficients $a_{l,n}$ for negative values of n *a posteriori* using the relationships $a^R_{l,-n} = a^R_{l,n}$, $a^I_{l,-n} = -a^I_{l,n}$, with corresponding expressions for $b_{l,n}$. The Fourier operator

$$\frac{\beta}{2\pi} \int_0^{2\pi/\beta} dy e^{i\gamma\beta y}$$

is then applied to equations (11) and (12).

In order to obtain numerical solutions we truncate the series in expressions (23) and (24) at $l = L$ and $n = N$ and allow γ to take integer values from 1 to N. We also truncate the series in expression (25) at $k = K$, where in practice we always use $K = L$, and apply a Chebyschev collocation-point numerical technique by evaluating the remaining equations at the $L+1$ internal collocation points given by equation (22). This leads to $(L + 1)(4N + 1)$ real nonlinear equations of the form

$$F_n = D_{nm} X_m + H_{nmk} X_m X_k = 0, \quad n = 1, \ldots, (L + 1)(4N + 1), \tag{26}$$

where the summation convention has been used and X_m, $m = 1, \ldots, (L + 1)(4N + 1)$ represents the solution vector containing the $4N(L + 1)$ unknown real and imaginary parts of the coefficients $a_{l,n}$ and $b_{l,n}$, and the $L + 1$ unknown real coefficients C_k, $k = 0, \ldots L$. The number of coefficients can be further reduced by approximately a half if symmetries are applied. Specifically, it is sufficient to consider solutions in the following set of modes:

Φ	Ψ
$\cos(n''\beta y) f_{l''}(z)$	$\cos(n'\beta y) g_{l''}(z)$
$\cos(n''\beta y) f_{l'}(z)$	$\cos(n'\beta y) g_{l'}(z)$
$\sin(n'\beta y) f_{l''}(z)$	$\sin(n''\beta y) g_{l''}(z)$
$\sin(n'\beta y) f_{l'}(z)$	$\sin(n''\beta y) g_{l'}(z)$,

where a double prime attached to l or n denotes an even integer, while a single prime denotes an odd integer, with $f_l(z) = T_l(z)(1 - z^2)^2$ and $g_l(z) = T_l(z)(1 - z^2)$. We solve the nonlinear algebraic system of equations (26) using the Newton–Raphson iteration method. Most of our results were obtained with the truncation levels $L = 15$ and $N = 7$, at which level the solution appears to be adequately converged, with the relative error in the leading-order coefficients $O(10^{-3})$ by comparison with a numerical solution at a much higher truncation level. Generally speaking, we found that a higher truncation level was required to maintain the same level of accuracy with increasing R, while some problems were encountered in following a particular solution

L	N	$a^R_{0,1}$	$L_2(\phi)$
11	5	0.144500793×10^1	0.269256322×10^1
11	6	0.143220807×10^1	0.266463549×10^1
11	7	0.143316270×10^1	0.266676600×10^1
11	9	0.143310594×10^1	0.266664783×10^1
15	7	0.143128335×10^1	0.267176575×10^1
15	8	0.143121899×10^1	0.267163155×10^1
15	9	0.143122018×10^1	0.267163492×10^1
17	8	0.143045099×10^1	0.267085170×10^1
19	9	0.143052520×10^1	0.267102985×10^1
27	9	0.143055870×10^1	0.267103346×10^1
29	11	0.143055776×10^1	0.267103544×10^1

TABLE 1. Convergence of the real part of the leading-order ϕ coefficient, $a^R_{0,1}$, and the L_2 norm of the ϕ amplitude coefficients $a_{l,n}$, $L_2(\phi)$, for the truncation levels indicated for the upper-branch solution when $R = 3000$, $\beta = 5$ and $\Omega = 22.1325$.

branch in regions of phase space in which two branches for the same parameters existed in close proximity, for example the AB and DE $\beta = 1.25$ branches of figure 6. A higher truncation level together with smaller steps along the solution branch overcame this problem. For reference, the turning point on the $\beta = 5$ branch shown in figure 6 is found to be 4130.6, 4126.7 and 4127.9 for truncation levels ($L = 15$, $N = 7$), ($L = 17$, $N = 9$) and ($L = 23$, $N = 10$) respectively. Table 1 displays convergence of the secondary flow at various truncation levels for another higher Reynolds number flow.

4.2. *Results*

In figure 6 we have plotted values of the L_2 norm of the amplitude coefficients $a_{l,n}$ in parameter space against R for various spanwise wavenumbers when $\Omega = 22.1325$. The marginal stability points derived by the linear stability analysis of the preceding section correspond to the bifurcation points of the nonlinear solutions from the basic flow, where $L_2(a_{0,1}, \ldots, a_{L,N}) = 0$. If we consider the solution for $\beta = 2.5$, it may be observed that the solution bifurcates from the basic flow in a supercritical bifurcation, with the amplitude of the bifurcating solution increasing with increasing R until a turning point is reached at $R \approx 374$ (equivalent to $Re^{AP} = 408$, $Rot^{AP} = 0.109$). The amplitude then decreases as R reduces until, at $R \approx 153$, the solution appears to merge with that of the upper branch of the $\beta = 5$ solution shown in figure 6. In fact, on applying linear secondary stability analysis as described in § 5 to the $\beta = 5$ solution, it is clear that at this point a single real eigenvalue changes sign, which corresponds to a steady, subharmonic bifurcation in agreement with the nonlinear results. We illustrate the transition from the $\beta = 5$ solution branch to the $\beta = 2.5$ solution branch via this bifurcation in figure 7 by displaying a visualization of contours of ϕ. As may be seen in the figure, such a bifurcation, in which the spanwise wavelength of the flow doubles, corresponds to a merging of some of the vortical structures present in the $\beta = 5$ case. In figure 7(a) we show contours of ϕ on the $\beta = 5$ branch slightly below the bifurcation point. Note that in general, as shown in this figure, the fluctuating variables tend to be concentrated in the $z > 0$ half of the channel. This is in agreement with the basic inviscid local instability criterion described by Pedley (1969) or Bradshaw (1969), which yields instability when

$$2\Omega^*(\mathrm{d}U/\mathrm{d}z^* - 2\Omega^*) > 0,$$

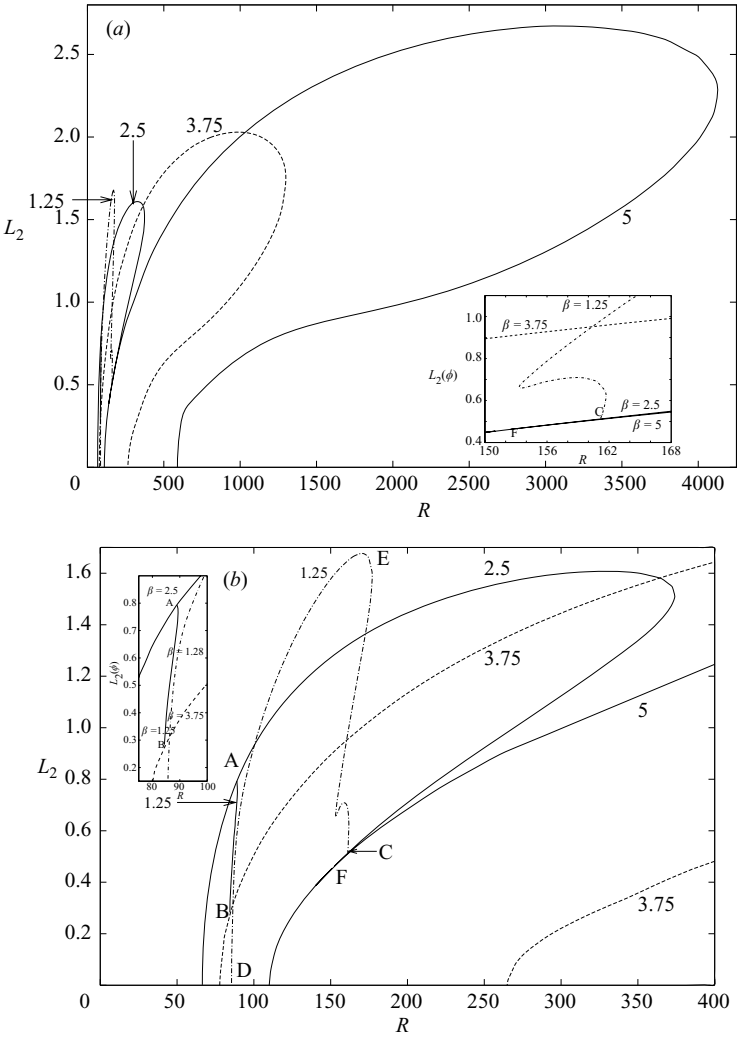

FIGURE 6. Amplitude of the bifurcating secondary flows against R when $\Omega = 22.1325$ and the values of β indicated. Enhanced detail of full plot (a) is shown in plot (b) and in the insets.

where U is the mean velocity (this is equivalent to the sign of the Bradshaw number, the product of relative spanwise and absolute spanwise vorticity, being positive). For the present case, for which $\Omega^* < 0$, instability may therefore occur in the $z^* > 0$ half of the channel according to this criterion. At slightly beyond the bifurcation point, on the $\beta = 2.5$ branch as shown in figure 7(b), it can be seen that the vortices marked A in the $\beta = 5$ pre-bifurcation solution figure 7(a) are strengthening in the post-bifurcation solution, whereas the vortices labelled B are disappearing, with those marked C coalescing to form a streamwise-invariant structure of horseshoe cross-section in figure 7(c). A larger distance away from the bifurcation point on the $\beta = 2.5$ branch, as shown in figure 7(d), the flow assumes a more familiar streamwise-vortex appearance similar to that of the pre-bifurcation solution shown in figure 7(a). However, in comparison with the latter solution, the centres of the vortices have shifted to be closer to the channel centreline while the wavelength of the flow has of course doubled.

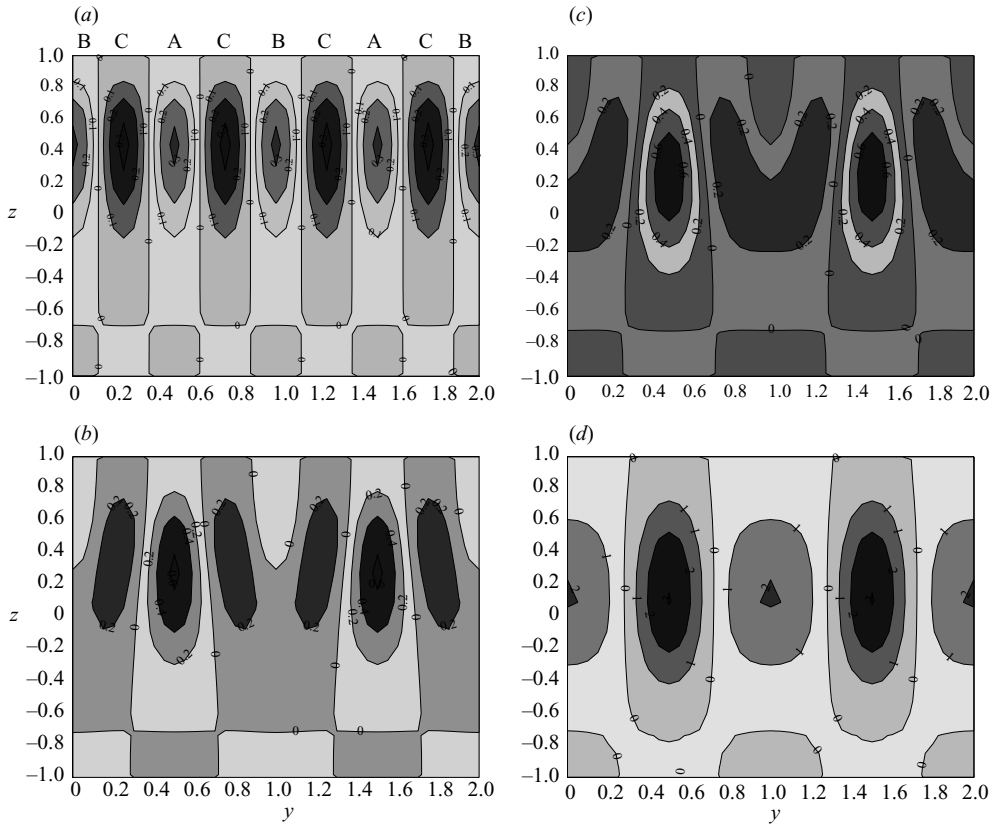

FIGURE 7. Contours of ϕ when $\Omega = 22.1325$ at (*a*) $R = 150$ on the $\beta = 5$ solution branch, which bifurcates at $R \approx 152.5$ to a $\beta = 2.5$ branch shown at (*b*) $R = 156$, (*c*) $R = 160$ and (*d*) $R = 374$. All plots have been scaled to show two spanwise wavelengths on the $\beta = 2.5$ scale, and were obtained with $L = 15$ and $N = 7$.

In contrast to the $\beta = 2.5$ solution bifurcating from the basic flow, the $\beta = 5$ branch shown in figure 6, after similarly reaching a turning point at $R \approx 4128$ (equivalent to $Re^{AP} = 3295$, $Rot^{AP} = 0.0134$), then, however, reconnects with the basic flow at $R \approx 589$. Linear stability analysis of the basic flow, as described in § 3, demonstrates that this point corresponds to a marginal stability point arising from the change in sign of the second most unstable eigenvalue, which is also real.

If we consider now the solution for $\beta = 1.25$, we see a behaviour distinct from the previous cases. The secondary flow bifurcates in a supercritical bifurcation with the amplitude of the secondary flow first increasing with R along an upper bifurcation branch until a turning point is reached at $R \approx 177$. Amplitude then decreases as the solution follows a lower branch. However, in this case, a further two turning points in R are reached before the solution branch finally terminates on the $\beta = 2.5$ lower branch at point C, near to this branch's own bifurcation from the $\beta = 5$ upper branch at point F in figure 6. The stability analysis described in § 5 applied to the $\beta = 2.5$ solution shows that the bifurcation at point C corresponds to a steady subharmonic bifurcation when a real eigenvalue, the third most unstable, changes sign.

In fact secondary stability analyses demonstrate that many solution branches may exist for lower values of β owing to the possibility of subharmonic bifurcation from

flows with larger β. Indeed, given that every secondary flow appears to lose stability to spanwise instabilities of any wavenumber, as will be described in § 5, we would expect an uncountable number of solution branches corresponding to small spanwise wavenumbers. For reference, we have included another solution for $\beta = 1.25$ in figure 6. In this case the solution bifurcates from the $\beta = 2.5$ upper branch at $R \approx 89$, point A in the figure, with the bifurcating branch reaching a turning point at $R \approx 89.3$ before the amplitude of the bifurcating solution continues to decrease to a termination point B on the $\beta = 3.75$ upper branch. Secondary stability analysis confirms that this point corresponds to a one-three mode steady subharmonic bifurcation from the $\beta = 3.75$ to $\beta = 1.25$ branch. We have visualized the transition from the $\beta = 2.5$ solution at point A to the $\beta = 3.75$ solution at point B via this $\beta = 1.25$ connecting branch by plotting contours of ψ in figure 8. All the spanwise plots have been scaled to contain one wavelength on the $\beta = 1.25$ scale. Thus in figure 8(a), which plots the $\beta = 2.5$ branch at the bifurcation point A marked on figure 6, two wavelengths of the solution are shown and four vortices are visible in the upper half of the channel. As we move onto the $\beta = 1.25$ branch, figure 8(b), four vortex structures are initially retained, but the doubling of the wavelength is clearly visible; none of the vortices are identical. As we continue to progress down the $\beta = 1.25$ branch, as shown in figure 8(c, d), the two vortices at either spanwise edge of the plotted domain gather strength at the expense of the two inner vortices, while in figure 8(d) the beginning of an additional pair of vortices is just apparent in the upper corners of the plotted domain. These have strengthened in figure 8(e) to form a total of six vortices across the spanwise width of the domain shown. Finally, in figure 8(f), the solution on the $\beta = 3.75$ branch close to the bifurcation point shows six vortices of equal strength, comprising three spanwise wavelengths of this solution.

In figure 9 we plot profiles of the mean flow at various points on the upper and lower branches of the $\beta = 5$ solution shown in figure 6. It may be seen that as we move away from the bifurcation point the flow loses the parabolic profile of the basic flow, and develops a flat profile which is in general slightly skewed into the half of the channel that is unstable according to the inviscid stability criterion. If, as is undertaken in figure 10, the corresponding absolute vorticity profiles (i.e. profiles of the vorticity of the mean flow in an inertial reference frame) are considered, we observe that this quantity approaches zero across a wide region in the centre of the channel as R increases. In such a region the flow is neutrally stable according to inviscid stability theory. We note that this phenomenon has also been found in the numerical simulations of turbulent flows by Kristoffersen & Andersson (1993), and also in the experiments of Johnston, Halleen & Lezius (1972). It may be noted that, by contrast, the flow near the lower-branch bifurcation point from the basic flow at $R = 595$ exhibits an absolute vorticity profile that is nearly linear, in agreement with expectations.

5. Stability of the secondary flow

It is of interest to determine the linear stability of the nonlinear secondary flows in order to give information on which of these flows may be observed in practice, and also to give information about the bifurcating tertiary flow. In the present study we will consider the stability of the secondary flow to three-dimensional secondary disturbances, which includes the special cases of streamwise-independent and spanwise-independent disturbances considered in the studies of Guo & Finlay (1991) and Finlay (1990) respectively. Accordingly, we consider a three-dimensional

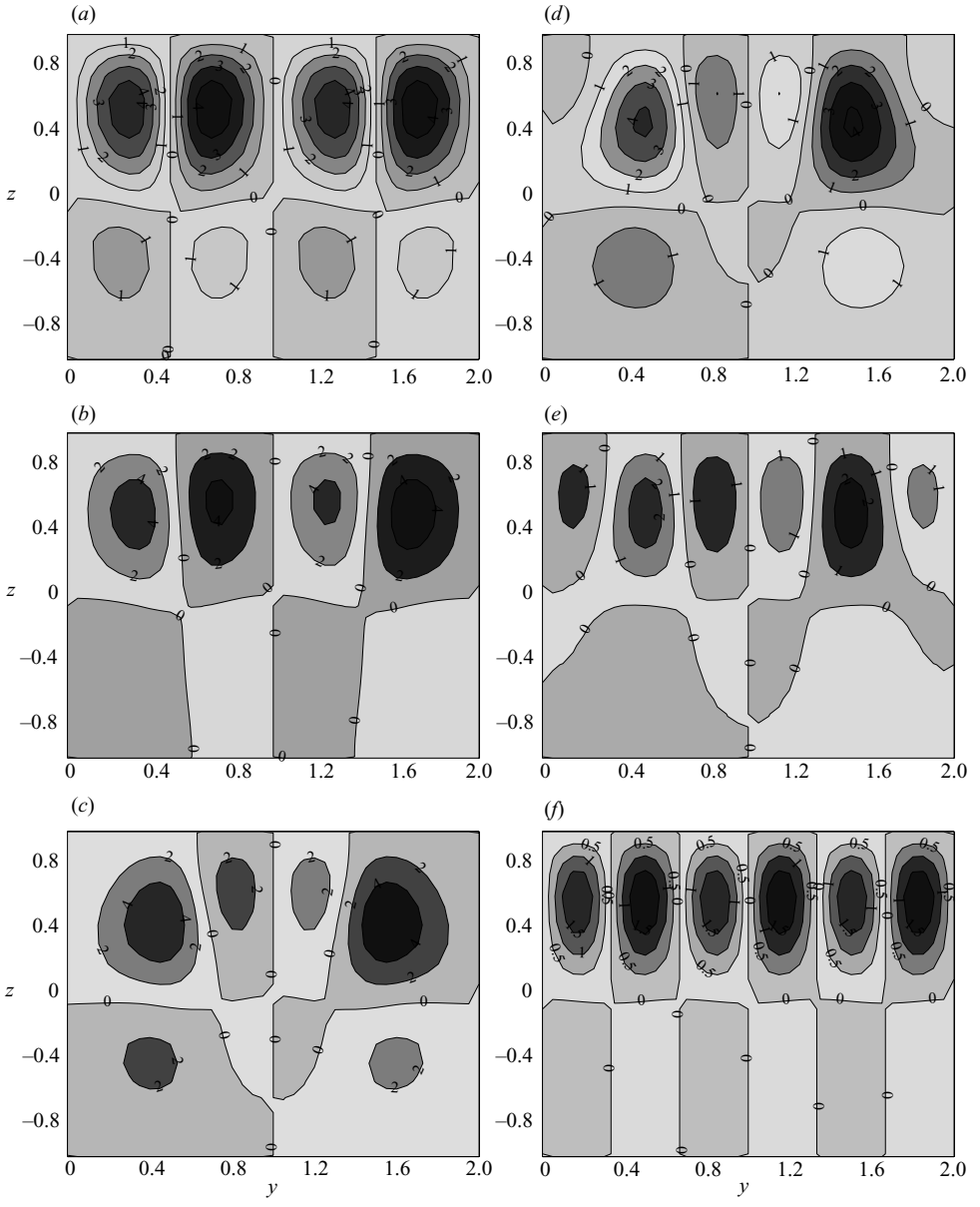

FIGURE 8. Contours of ψ when $\Omega = 22.1325$, on (a) the $\beta = 2.5$ solution branch at the point $R = 88.95$ of bifurcation to the $\beta = 1.25$ branch (b) and (c) $R = 89$, (d) $R = 86$, (e) $R = 84.45$ which then terminates on (f), the point of bifurcation from the $\beta = 3.75$ solution at $R = 84.3$. Truncation levels $L = 15$, $N = 7$ (a, f) and $L = 23$, $N = 8$ (b–e) were used.

disturbance, $\boldsymbol{u} = \tilde{\boldsymbol{u}}(x, y, z, t)$ and $p = \tilde{p}(x, y, z, t)$, and the total flow $\boldsymbol{u} = U_0\boldsymbol{i} + \hat{\boldsymbol{u}} + \tilde{\boldsymbol{u}}$, $p = p_0 + \hat{p} + \tilde{p}$, must satisfy the governing equations (2)–(3) subject to boundary conditions (4).

Since the disturbance is solenoidal, we may decompose it according to $\tilde{\boldsymbol{u}} = \nabla \times (\nabla \times \tilde{\phi}\boldsymbol{k}) + \nabla \times \tilde{\psi}\boldsymbol{k}$, and apply the operators $\boldsymbol{k} \cdot \nabla \times$ and $\boldsymbol{k} \cdot \nabla \times (\nabla \times$ as before. Since we are here concerned with the linear stability of the secondary flow, products

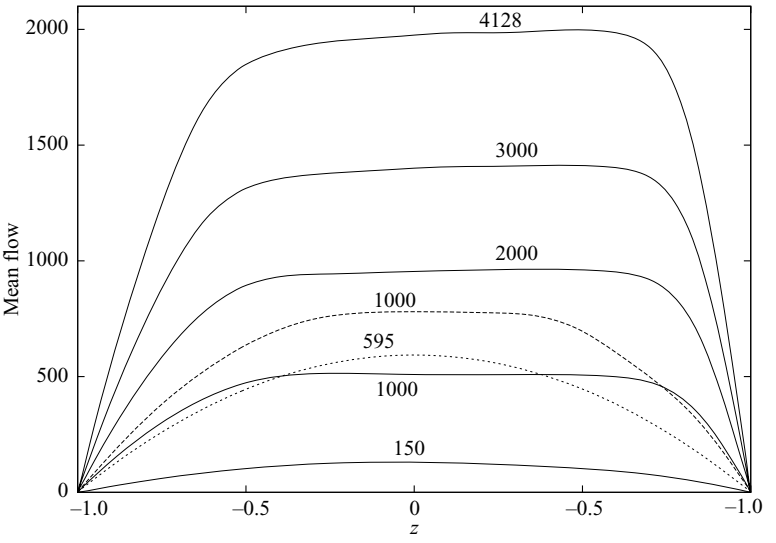

FIGURE 9. Mean flow $U = u_0 + \breve{U}$ at the values of R indicated when $\Omega = 22.1325$ and $\beta = 5$ on the upper branch (—), the lower branch (- -).

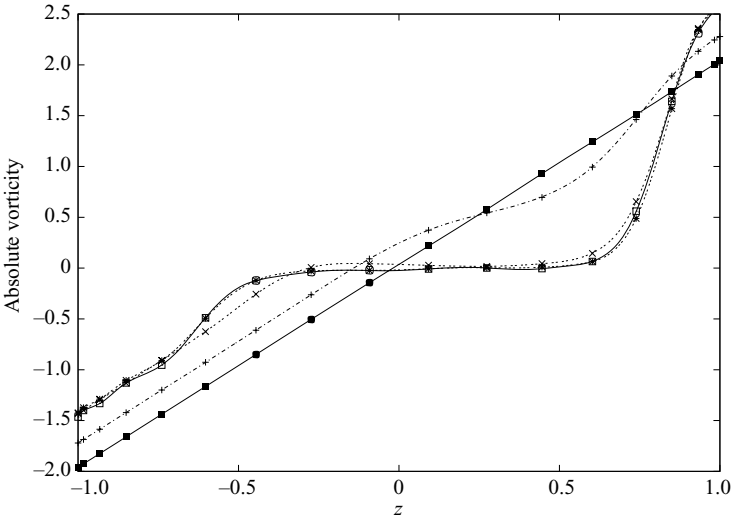

FIGURE 10. The absolute vorticity $(\Omega - \mathrm{d}U/\mathrm{d}z)/R$ when $\Omega = 22.1325$ and $\beta = 5$ at the values of R: on the upper branch, 150 (+), 1000 ($\times$), 3000 (*), 4128 (□); and the lower branch, 595 (■).

of the secondary disturbance are discarded, and Floquet theory encourages us to seek solutions in the form

$$\tilde{\phi} = \sum_{l=0}^{\infty} \sum_{n=-\infty}^{\infty} \tilde{a}_{l,n} \mathrm{e}^{\mathrm{i}n\beta y + \mathrm{i}dx + \mathrm{i}by + \sigma t} T_l(z)(1 - z^2)^2, \tag{28}$$

$$\tilde{\psi} = \sum_{l=0}^{\infty} \sum_{n=-\infty}^{\infty} \tilde{b}_{l,n} \mathrm{e}^{\mathrm{i}n\beta y + \mathrm{i}dx + \mathrm{i}by + \sigma t} T_l(z)(1 - z^2), \tag{29}$$

L	N	σ_1^R
15	7	$-0.191133542767 \times 10^{-1}$
19	7	$-0.191127549476 \times 10^{-1}$
23	7	$-0.191127398838 \times 10^{-1}$
27	7	$-0.191127403631 \times 10^{-1}$
15	8	$-0.191133541371 \times 10^{-1}$
23	8	$-0.191126932456 \times 10^{-1}$
27	9	$-0.191127393360 \times 10^{-1}$

TABLE 2. Convergence of σ_1^R against truncation level for the upper-branch flow with $R = 80$, $\Omega = 22.1325$ and $\beta = 2.5$ subject to a disturbance with $d = 0$ and $b = 0.3$.

where d and b are real Floquet parameters which we may assume are non-negative without loss of generality, and σ is the disturbance growth rate. For given values of R, β, Ω, d and b, adopting the same eigenvalue labelling convention as in § 3, if $\sigma_1^R > 0$ the flow is unstable, while if $\sigma_1^R < 0$ the flow is stable. If $\sigma_1^R = 0$ the flow is neutrally stable, and these points offer a possible bifurcation point for the tertiary flow. We note that $\tilde{\phi}$ and $\tilde{\psi}$ are periodic in the Floquet parameter b with period β, and so it is therefore necessary and sufficient to examine the semi-infinite strip $0 \leqslant b < \beta$ in Floquet parameter space at each point on the secondary-flow bifurcation branch in order to determine the stability of the secondary flow at that point. Results are also symmetric about $b = \beta/2$, as discussed by Nagata & Busse (1983), although some of our results were calculated in the full strip $0 \leqslant b < \beta$ in order to check the rectitude of the stability code. Equations for the unknown coefficients $\tilde{a}_{l,n}$ and $\tilde{b}_{l,n}$, and the eigenvalue σ are derived by applying the operator

$$\frac{\alpha\beta}{4\pi^2} e^{-\sigma t} \int_0^{2\pi/\alpha} dx e^{-idx} \int_0^{2\pi/\beta} dy e^{-i\{\gamma\beta y + by\}}.$$

5.1. *Numerical method*

Upon varying γ over the values $-N$, $-N+1, \ldots, N$ and evaluating the resultant equations at the $L+1$ internal collocation points given by equation (22), we obtain a system of $2(L+1)(2N+1)$ equations which form a generalized algebraic eigenvalue problem of the form $A\boldsymbol{x} = \sigma B\boldsymbol{x}$, for the eigenvalues σ with eigenvector $(\tilde{a}_{0,-N}, \tilde{a}_{0,-N+1}, \ldots, \tilde{a}_{0,N}, \tilde{a}_{1,-N}, \ldots, \tilde{a}_{L,N}, \tilde{b}_{0,-N}, \ldots, \tilde{b}_{L,N})$. We solve this eigenvalue problem using the QZ algorithm, and for most of our results for the most unstable eigenvalue we used $L = 15$ and $N = 7$, but higher truncation levels are required for lower-order eigenvalues. Table 2 shows convergence of the most unstable eigenvalue against truncation level for a test problem.

5.2. *Results*

In order to fully consider the stability of a given streamwise-independent flow, we consider stability to disturbances of all Floquet parameter values within the semi-infinite strip $0 \leqslant b < \beta$, $0 \leqslant d$ due to the periodicity of b described earlier. We first consider the stability of the $\beta = 2.5$ secondary flow branch shown in figure 6. We consider the stability of this flow at a sequence of points along the upper and lower solution branches. The results are presented in figure 11, where we plot contours of the real part of the most unstable eigenvalue in Floquet parameter space. It may be seen in figure 11(*a*) that when $R = 70$ the secondary flow is stable to all

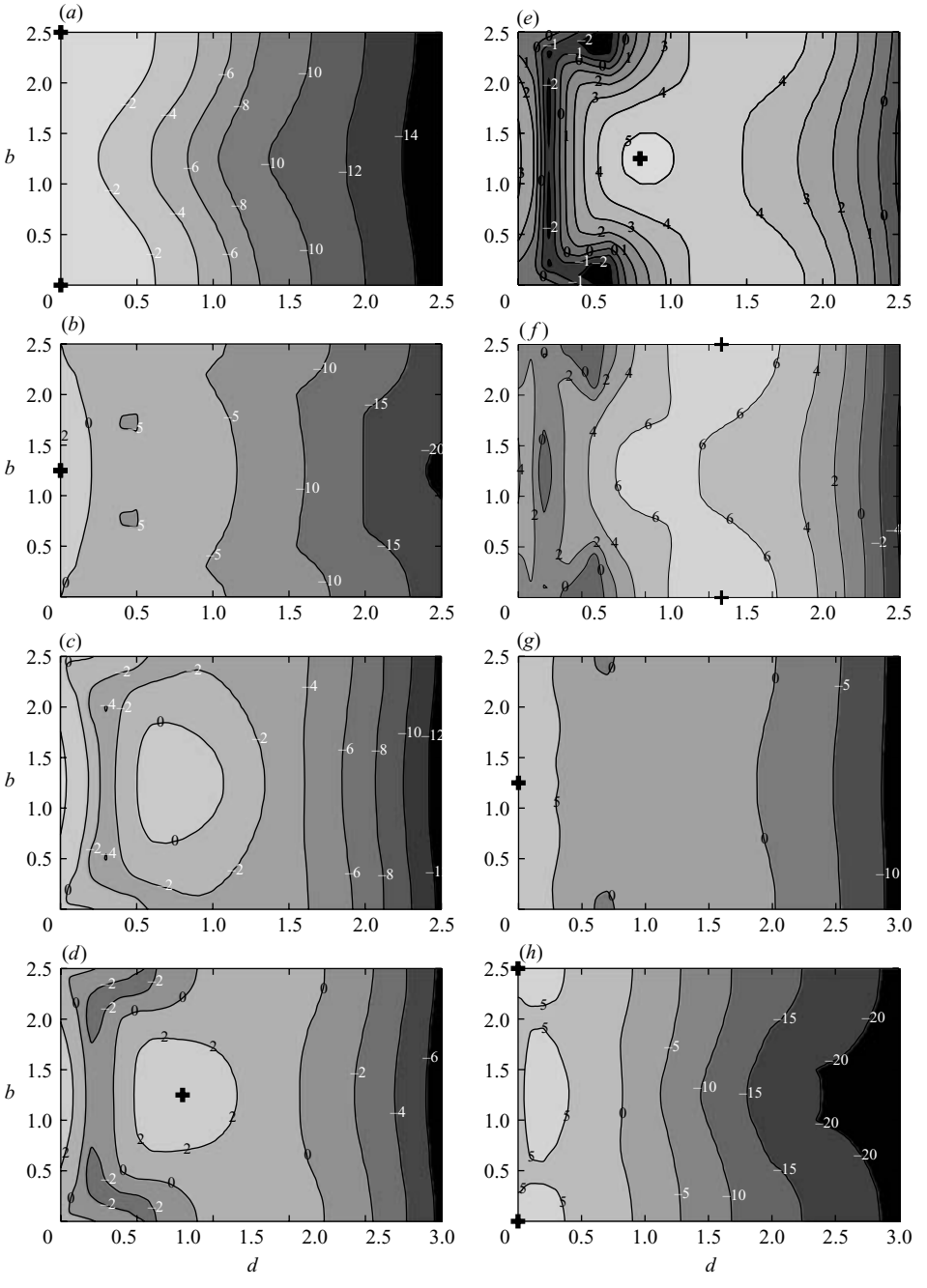

FIGURE 11. Contours of the real part of the most unstable eigenvalue in Floquet parameter space for the secondary flow bifurcating directly from the basic state with $\beta = 2.5$, $\Omega = 22.1325$ on the upper branch at (*a*) $R = 70$, (*b*) $R = 130$, (*c*) $R = 220$, (*d*) $R = 280$, (*e*) $R = 340$ and (*f*) $R = 374.1$, and on the lower branch at (*g*) $R = 310$ and (*h*) $R = 160$ for truncation level $L = 15$, $N = 7$. In each figure the cross (+) denotes the location of the mode with largest growth rate.

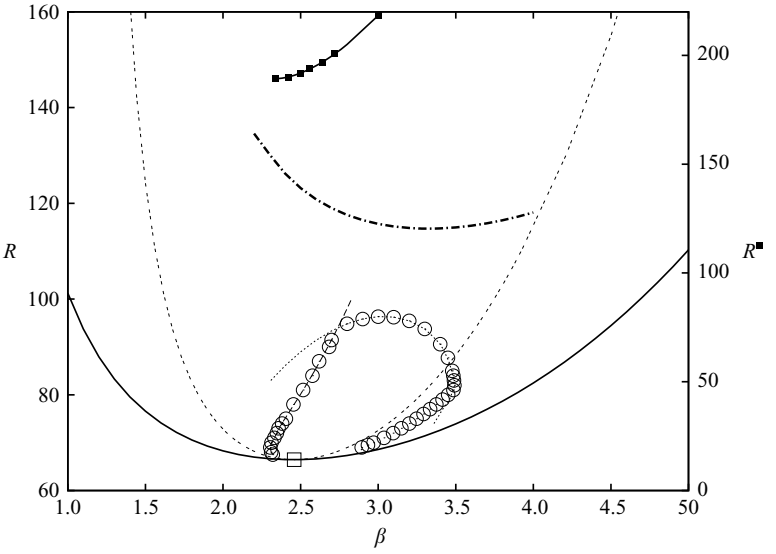

FIGURE 12. The linear marginal stability curve (—) together with the Eckhaus secondary stability boundary (○) for β against R when $\Omega = 22.1325$, together with contours of $\sigma_1^R = 0$ for vanishing b (- - -) and $b = \beta/2$ ($\cdots$). Eckhaus's (1965) approximation (- - - -) is also plotted, and the linear critical point is marked by a box (□). We also show the secondary marginal stability curve for the $d = 0.1, b = 0$ mode (-·-) and, on the right-hand ($R^{\blacksquare}$) axis, the first appearance of the three-dimensional subharmonic secondary stability mode (disjoint from the region associated with the Eckhaus mode) (—■—). The secondary stability results were obtained at truncation level $L = 15$, $N = 7$.

disturbances, and hence may be expected to be realized both in numerical simulations as well as experimentally. In fact our calculations show that this flow is stable to all disturbances for $R \leqslant 80$, at which point the flow loses stability to a disturbance with $d = 0$ and vanishing b, with the corresponding eigenvalue real. We will call secondary disturbance modes with $d = 0$ Eckhaus modes, and discuss the stability of these modes, Eckhaus instability, later in this section.

As R increases, as may be seen with reference to figure 11(b), the flow rapidly becomes unstable to all values of $b \in (0, \beta)$ for zero d, with the subharmonic secondary-disturbance modes $b = \beta/2$ possessing the largest growth rates. The region of unstable Floquet parameter values also expands from the $d = 0$ axis to include disturbances with small d and non-zero b.

When R reaches 220 on the upper branch, two additional unstable modes appear. First, the flow becomes unstable to a mode with zero b and small d which is initially a disjoint region in Floquet space (as may be seen in figure 15 for different parameters), but then joins with the Eckhaus-unstable region. The corresponding wave speed is non-zero. We have plotted a secondary marginal stability curve for the mode $d = 0.1, b = 0$ in R, β space in figure 12; this mode first appears for $R \approx 120$, $\beta \approx 3.32$.

A second instability mode then also appears, which may be seen in figure 11(c) as the disjoint region of instability centred around $d \approx 0.75$ and $b = 1.25$. As R increases it may be seen with reference to figure 11(d) that such a three-dimensional spanwise-subharmonic disturbance ($d \neq 0$, $b = \beta/2$) then becomes the disturbance of largest growth rate. This mode consists of a single complex eigenvalue, and so would

be expected to produce a travelling-wave tertiary flow. With reference to figure 11(*d*, *e*), it can be seen that this second region of unstable Floquet parameters eventually extends to include all spanwise Floquet parameters. It can also be seen that upon reaching the turning point, figure 11(*f*), the mode with largest growth rate has become one with $b = 0,\ d > 0$ (recall that σ is periodic in b with period β).

From the turning point of the nonlinear branch, as we progress down the lower branch it may be seen in figure 11(*g*, *h*), that the region of instability then collapses to a single region which is bounded by a finite value of d. The flow remains unstable everywhere on the lower branch. The second most unstable mode first becomes unstable at the turning point of the nonlinear solution branch ($R = 374.1$).

Eckhaus instability describes the stability of a supercritically bifurcating two-dimensional nonlinear solution to two-dimensional disturbances, where these disturbances are functions of the cross-channel ordinate, and periodic functions of the other space variable on which the bifurcating nonlinear flows depend. In the present case, these two-dimensional disturbances are the Eckhaus modes defined earlier in this section, and are thus periodic in the spanwise direction, and streamwise independent. Eckhaus (1965) used an amplitude expansion method to derive an approximation for the band of wavenumbers stable to Eckhaus disturbance modes in the vicinity of the linear critical point,

$$\frac{\beta_L^m(R) - \beta_c}{\sqrt{3}} < \beta - \beta_c < \frac{\beta_R^m(R) - \beta_c}{\sqrt{3}}, \tag{30}$$

where $\beta_L^m(R)$ and $\beta_R^m(R)$ denote the left- and right-hand branches of the linear marginal stability curve respectively. In figure 12 we have shown where the nonlinear flow bifurcating from the critical point is stable in the (R,β)- plane. The flow bifurcates supercritically from the linear marginal curve in a region about the critical point, and the stability of the resultant nonlinear secondary flow is then determined by its stability to Eckhaus-type modes ($d = 0$) since, in all our results, the flow always loses stability to disturbances of this kind first with increasing R. Tracing a marginal stability curve for these disturbances for this flow it appears to produce a closed region of stable flows. We note that the most unstable Eckhaus mode, whose real part's change in sign forms the Eckhaus boundary plotted in the figure, always has a zero imaginary part. As may be seen with reference to the contours plotted in the figure, most of the left-hand boundary is determined by $b = 0$, while the upper parts of the left- and right-hand Eckhaus boundaries are determined by the subharmonic $b = \beta/2$ mode. The lower part of the right-hand Eckhaus boundary is then determined by values of b decreasing towards 0 as β decreases. We have also included a plot of Eckhaus's (1965) approximation (30); clearly this approximation does not correctly describe the Eckhaus stability characteristics of the present problem, as Guo & Finlay (1991) also found for flow through a curved channel. We note also that it may be seen from the diagram that the solutions bifurcating from the basic state when $\Omega = 22.1325$ for $\beta = 1.25$ and 5 shown plotted in figure 6 are, in particular, unstable from point of bifurcation from the basic state and never become stable with increasing R. However, as noted in the Introduction, these flows may nonetheless be important in explaining features of coherent structures in turbulent flow.

As well as providing information about the stability of the secondary flows, secondary stability analysis also allows bifurcation points for the tertiary flow to be identified, and yields some information regarding the nature of the bifurcating solution. In our analyses we have been able to identify four distinct types of bifurcation: (i) $d = 0,\ b \neq 0$, a single real eigenvalue crosses the real axis with

$\sigma_I = 0$, (ii) $b = 0$, $d \neq 0$, a single eigenvalue crosses the real axis with $\sigma_I \neq 0$, (iii) $d \neq 0, b \neq 0$, a single eigenvalue crosses the real axis with $\sigma_I \neq 0$ and (iv) $b \neq 0$, a complex-conjugate pair of eigenvalues crosses the real axis. A bifurcation of type (i) will produce a steady streamwise-independent bifurcating flow of the same form as the secondary flows of the present study. This type of bifurcation corresponds to the bifurcation of the upper branch of the $\beta = 5$ solution to the lower branch of the $\beta = 2.5$ solution at point F in figure 6, as well as the bifurcation from the $\beta = 2.5$ solution at point C to the $\beta = 1.25$ solution bifurcating from the basic flow, and also occurs at both ends A and B of the other $\beta = 1.25$ solution shown. Bifurcations of type (ii) and (iii), which will produce a travelling-wave solution, offer a possible route for obtaining the travelling-wave tertiary flows found in the DNS and experimental studies, which we discuss further in § 6. Both of these bifurcations lead to a streamwise-dependent tertiary flow, while for case (iii) the spanwise wavelength of the flow is also changed.

We can gain a further insight into the tertiary flows originating from some of the bifurcation types described above by constructing an approximate visualization by superimposing the secondary disturbance on the secondary flow. Such a visualization is carried out in figure 13 (*a*), where we show contours of the fluctuating component of velocity in the streamwise direction, u, and the streamwise component of the vorticity, $\boldsymbol{\omega}_x = [\nabla \times \boldsymbol{u}]_x$ for a bifurcation of type (ii) for parameters expected to lead to a flow of Finlay's (1990) WVF1 type. It may be seen that the flow is characterized a sequence of staggered vortices which elongate in the streamwise direction and lie either side of low-speed streaks in the streamwise velocity component.

In figure 13(*b*) we have also visualized a bifurcation of the same type which is expected to lead to a flow of the undulating wavy vortex type also discussed by Finlay (1990) (WVF2) and Alfredsson & Persson (1989). This undulating flow is qualitatively similar to the twisting one shown in figure 13, with again low-speed streaks in the streamwise velocity component lying between a set of staggered vortices in the x, z cross-section. In fact Finlay (1990) states that the two flows satisfy the same glide-and-reflect symmetries, and he distinguishes them by the differing amplitudes of motion and rocking of the vortices. For reference, plots depicting the structure of the tertiary flow in the vicinity of a subharmonic bifurcation point are shown in 13(*c*). The visualization has again been constructed by adding the eigensolution to the secondary flow. Clearly the structure is once more one consisting of a low-speed streamwise-orientated streak in the streamwise velocity component flanked either side by a set of vortices. However, in contrast to the superharmonic case, these vortices are aligned rather than staggered, and the profile of u is varicose rather than sinuous. A full nonlinear three-dimensional solution obtained by the bifurcation approach is necessary to provide a quantitative comparison between these flows and to investigate the form of the tertiary flows away from the vicinity of the bifurcation from the secondary flow. Visualizations of bifurcating three-dimensional tertiary flows for other parameter values we have considered exhibit the same qualitative patterns as those shown in figure 13.

6. Comparison with previous studies

Our findings appear to be in good qualitative agreement with those of previous experimental and DNS- based studies. In agreement with Alfredsson & Persson (1989), we have found that the basic flow first loses stability to two-dimensional, steady, streamwise-independent roll cells. Furthermore we have found that this streamwise-independent secondary flow is stable within a closed Eckhaus boundary, as was also

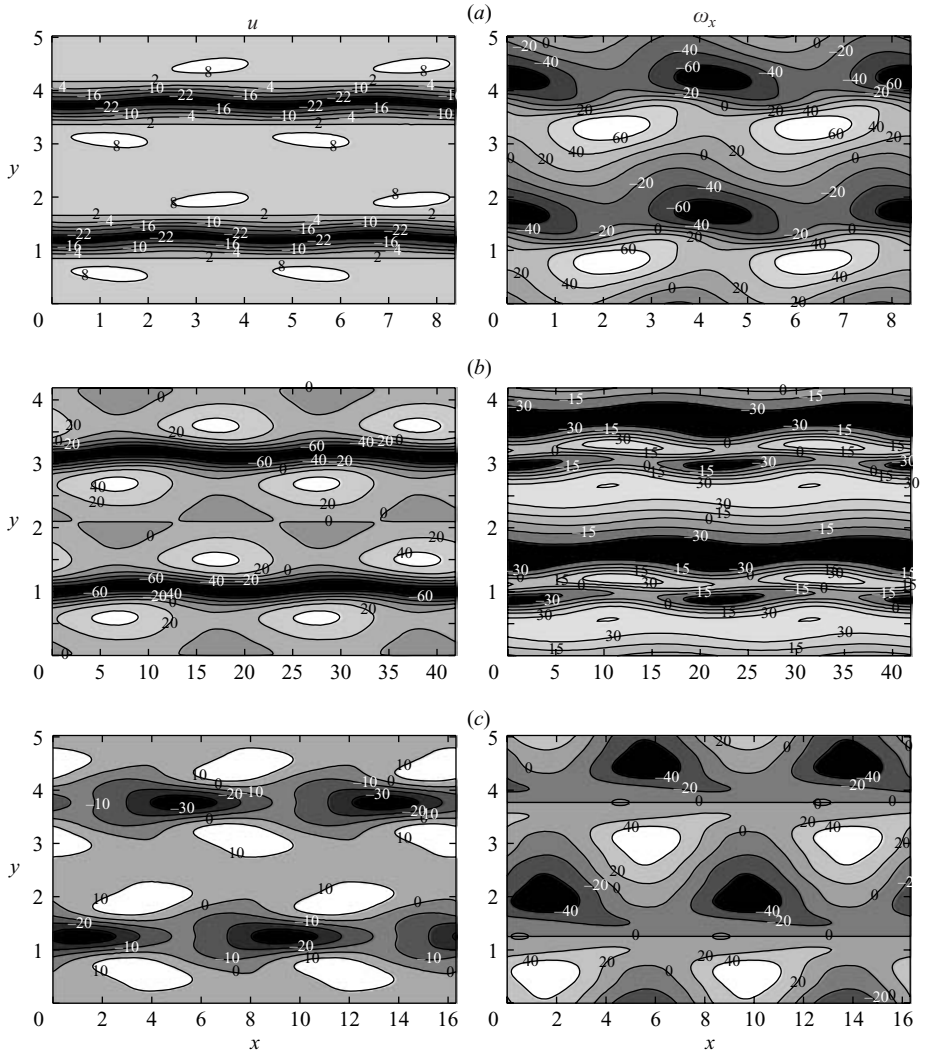

FIGURE 13. Left: contours of u, and right: contours of ω_x at $z = 0.85$ for (a) the solution approached by a tertiary flow with $\alpha = 1.5$, $\beta = 2.5$ and $\Omega = 22.1325$ in the limit as $R -> 268^+$ ($Re^{AP} = 294$, $Rot^{AP} = 0.151$); (b) an estimate of the tertiary flow structure when $\alpha = 0.3$, $\beta = 3.0$ and $\Omega = 27.5$ for $R = 532$ ($Re^{AP} = 550$, $Rot^{AP} = 0.1$); and (c) the solution approached by a tertiary flow with $\alpha = 0.77$, $\beta = 1.25$ and $\Omega = 22.1325$ in the limit as $R -> 192^+$ ($Re^{AP} = 216$, $Rot^{AP} = 0.205$). In all cases we have scaled the real part of the leading-order non-zero $\tilde{\phi}$ coefficient of the eigensolution ($\tilde{a}^R_{0,1}$ (a, b), $\tilde{a}^R_{0,0}$ (c)) to be $0.1\times$ the leading order ϕ coefficient of the two-dimensional nonlinear solution ($a^R_{0,1}$), with results obtained for truncation levels $L = 15$, $N = 7$ (b, c) and $L = 19$, $N = 7$ (a).

found by Guo & Finlay (1991), who considered the linear stability of a vortex flow generated by using a DNS code. We can also see this behaviour in the experimental study of Alfredsson & Persson (1989), for example their figure 5 shows the secondary flow losing stability to a steady streamwise-independent instability. We note that this property of the present secondary flows is in contrast to Taylor–Couette flows, whose corresponding Eckhaus boundary is open, see for example Nagata (1986).

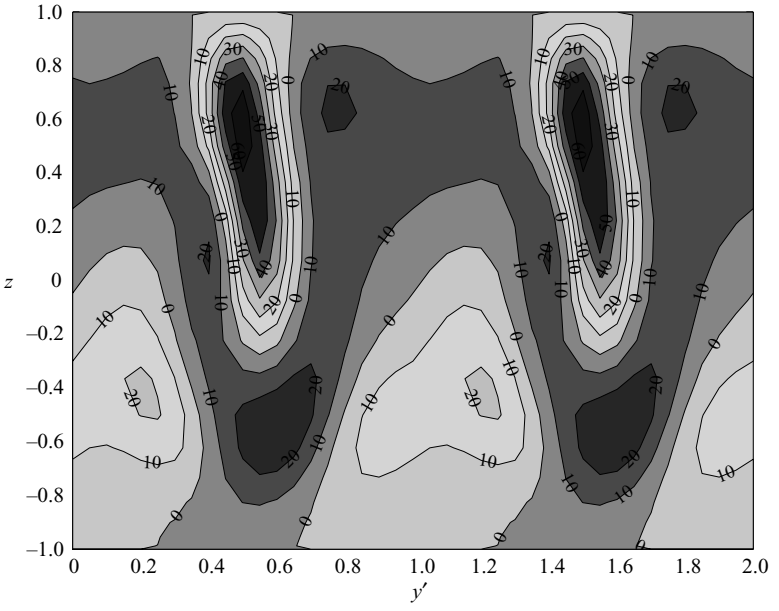

FIGURE 14. Contours of u for the solution approached by a tertiary flow with $\alpha = 1.5$, $\beta = 2.5$ and $\Omega = 22.1325$ in the limit as $R -> 268^{+}$. Results obtained for truncation level $L = 19$, $N = 7$. The figure has been scaled to show two wavelengths in the spanwise direction.

Moving beyond the Eckhaus boundary for fixed β, Ω as for the plots of figure 11, the instability mode with zero b and small d may correspond to Finlay's (1990) WVF2 or undulating flow. In particular, we find this eigenmode to be distinct from that which then appears at larger R with $b = 0$, $d = O(1)$. The latter mode appears to be consistent with Finlay's (1990) WVF1 and the twisting vortex flows described by Yang & Kim (1991) and Alfredsson & Persson (1989). In figure 14 we have plotted contours of u for the flow of figure 13 in the spanwise–wall-normal plane; although for different parameters, it bears a marked similarity to the plot of twisting vortices in Yang & Kim's (1991) figure 8. We also note that the WVF1 mode has appeared after WVF2, which Finlay (1990) found to be always the case when both are present. Of course, to confirm the relationship between these flows it will be necessary to compute the three-dimensional bifurcating flows and also analyse their stability.

We proceed now to make more precise quantitative comparisons with the results of some of these studies. Unless otherwise stated, where quantitative comparisons are made solutions of the present study lying on the upper branch of the flow bifurcating directly from the basic state will be used to compare with the previous work.

We sought to compare the results of the present study with the experimental results of Alfredsson & Persson (1989), considering first the results of the experiments shown in their figure 5. It may be noted that, owing to our differing choice of dimensions, values of R corresponding to the parameters used by Alfredsson & Persson (1989) for the streamwise-vortex secondary flow cannot be chosen *a priori* as they can for laminar flow, since flux is modified by the mean flow modification, $\breve{U}$. However, integrating $\breve{U}$ across the channel allows us to select R correctly. Accordingly, we examined the flows with (*a*) $R = 133.5$, $\Omega = 7.515$ and $\beta = 2.35$, (*b*) $R = 138.2$, $\Omega = 10.855$ and $\beta = 2.2$ and (*c*) $R = 143.3$, $\Omega = 14.195$ and $\beta = 2.65$ which correspond to Alfredsson & Persson's (1989) figures 5(*a*), 5(*b*) and 5(*c*) respectively. Performing a stability analysis

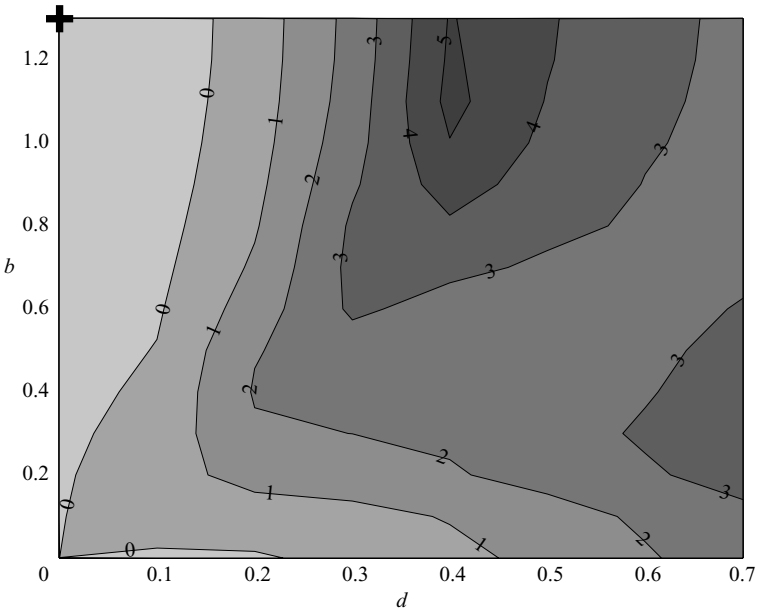

FIGURE 15. Contours of the real part of the most unstable eigenvalue in Floquet parameter space for the secondary flow corresponding to that in the experimental results of Alfredsson & Persson's (1989) figure 5(*c*), with $\beta = 2.65$, $\Omega = 14.195$ and $R = 143.3$ at truncation level $L = 15$, $N = 7$. The cross (+) denotes the location of the mode with largest growth rate.

of these three flows we find (*a*) to be stable to all disturbances, while for flows (*b*) and (*c*) there is a region of instability in the neighbourhood of the Eckhaus modes ($d = 0$) in Floquet parameter space. We have plotted contours of the real part of the most unstable eigenvalue for case (*c*) in figure 15. In both cases (*b*) and (*c*), the subharmonic Eckhaus mode $d = 0$, $b = \beta/2$ has the largest growth rate, while the corresponding imaginary part of the eigenvalue is zero. We therefore would expect a steady harmonic bifurcation to another streamwise-independent flow with double the spanwise wavelength. Our stability results would thus seem to appear to be in good agreement with the experimental findings included in Alfredsson & Persson's (1989) figure 5; the instability which Alfredsson & Persson (1989) describe may be observed by following a bright band from left to right in their figure and observing a splitting of this band into two separate bright bands. However, this instability only appears to be present in their figures 5(*b*) and 5(*c*), which is therefore in excellent agreement with the present stability results.

We further made a comparison with Alfredsson & Persson's (1989) figure 6(*d*), for which an equivalent flow in terms of the present dimensions is given by $R = 90.36$, $\Omega = 30.8$ and $\beta = 3.35$. We performed a secondary stability analysis of this flow and found it to be stable to for all values of d and b. This would again appear to be in full agreement with the experimental results since, in contrast to their figures 5(*b*) and 5(*c*), there does not appear to be any evidence of the spanwise bright-band splitting instability described above.

Finally, a comparison was made with the flow captured in figure 7(*b*) of Alfredsson & Persson's (1989) study, which depicts a streamwise-orientated flow losing stability to a three-dimensional travelling-wave disturbance which they describe as consisting of twisted roll cells. From the photograph we have estimated the spanwise wavenumber

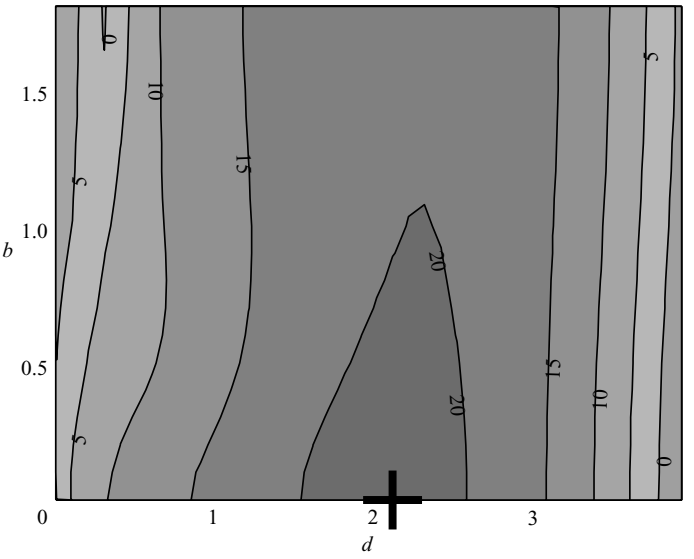

FIGURE 16. Contours of the real part of the most unstable eigenvalue in Floquet parameter space for the secondary flow corresponding to that in the experimental results of Alfredsson & Persson (1989) figure 7(*b*), with $\beta = 3.75$, $\Omega = 24.78$ and $R = 627.4$ at truncation level $L = 15$, $N = 7$. The cross (+) denotes the location of the mode with largest growth rate.

to be $\beta = 3.75$ in terms of the present dimensions, while selecting $\Omega = 24.75$ and $R = 627.4$ allows the other parameters to agree with those used by Alfredsson & Persson (1989). A plot of contours of the real part of the most unstable eigenvalue in Floquet parameter space is shown in figure 16. Clearly the flow is unstable to disturbances of a wide range of Floquet parameters including three-dimensional modes. However, the most unstable mode is a single complex eigenvalue with $b = 0$ and $d = 2.1$. This would suggest the growth of a three-dimensional flow consisting of a travelling wave imposed on the two-dimensional roll cells, in agreement with the experimental results. From Alfredsson & Persson's (1989) figure we estimate the observed streamwise wavenumber to be about 2.4, which is thus in reasonable agreement with the value, 2.1, derived from our stability analysis. The present study's predicted wave speed $c = -\sigma_1^I/d = 339$ is also in agreement with Alfredsson & Persson's (1989) study, which stated that the wave speed observed in their flows was of the order of half the undisturbed centreline velocity, which for this flow yields $c = 314$. A direct quantitative comparison with the experimental study of Matsubara & Alfredsson (1998) is difficult. This is because if we fix $\beta = 3.14$ and $\Omega = 16.9$ in order to agree with their parameter values, then the secondary flow bifurcating from the basic flow reaches a turning point at around $R = 960$, with the flux reaching $(1/2)\int u_0 + \breve{U}\,\mathrm{d}z = 485$, whereas the experiments are conducted at a flux of 650. However, we note that it is the sinuous form of tertiary flows shown in figure 13(*a*, *b*) that are consistent with the form of twisting travelling-wave flows studied by Matsubara & Alfredsson (1998).

We also made a quantitative comparison with the study by Finlay (1990), who used a three-dimensional DNS code to pick out the fastest growing eigenmodes after adding a wavy disturbance of normal-mode form to streamwise-independent vortex flows, which were also generated by a DNS code. The disturbances examined by Finlay (1990) correspond to those of the present study with $b = 0$. In figures 17 and 18, we have compared results for two different values of the rotation number used

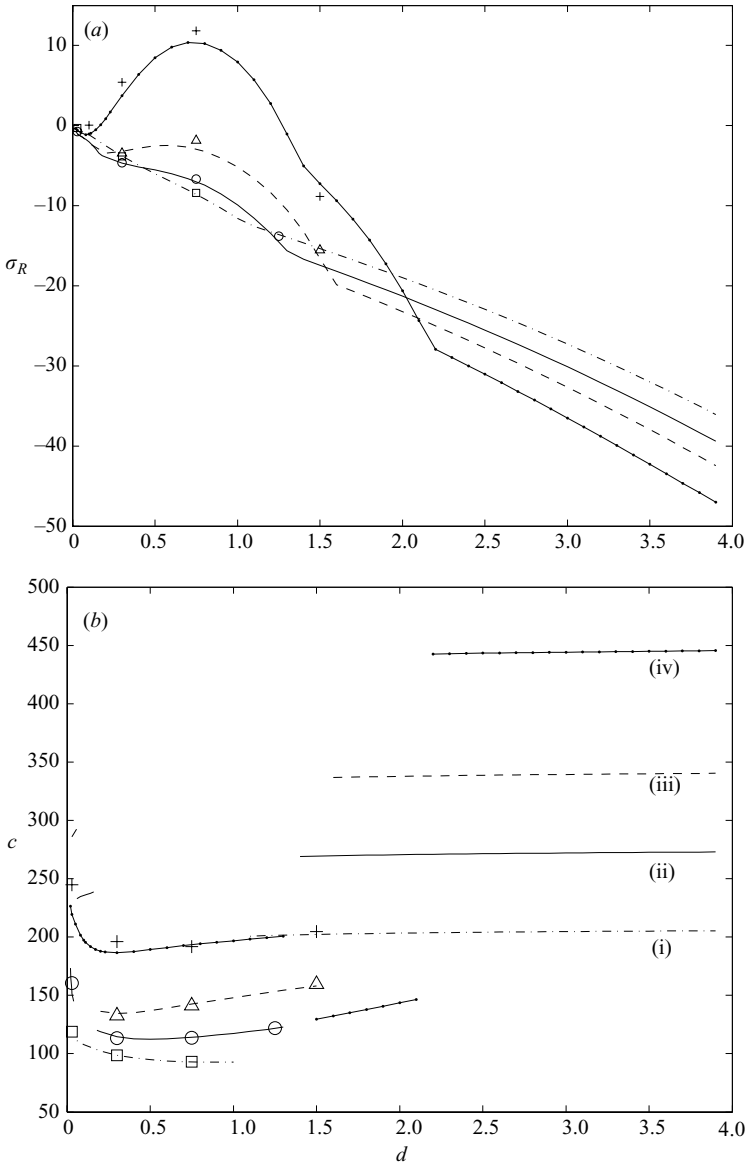

FIGURE 17. A comparison with Finlay's (1990) figures 2 and 3. (*a*) Growth rate and (*b*) wave speed against d (with $b=0$) for (i) $\Omega=210$, $\beta=5$ and $R=222.3$ (- · -); (ii) $\Omega=277.5$, $\beta=5$ and $R=299.4$ (–); (iii) $\Omega=345$, $\beta=5$ and $R=375.2$ (- -); and (iv) $\Omega=450$, $\beta=5$ and $R=491.6$ (—•—). All our results were obtained for truncation level $L=15$, $N=7$. Finlay's (1990) corresponding results are given by (i) □, (ii) ○, (iii) △ and (iv) +.

by Finlay (1990); figures 17(*a*) and (*b*) correspond to the case considered in Finlay's (1990) figures 2 and 3 respectively, while figures 18(*a*) and (*b*) correspond to the case considered in Finlay's (1990) figures 7 and 8 respectively. It can be seen from figure 17 that agreement with the values obtained by Finlay's (1990) alternative method are good, although marginally less so for the case with $\Omega=450$, $R=491.6$, particularly the wave speed for the smallest and largest data points in d. Agreement in figure 18 is also good, although again for these results agreement at the highest value of R seems

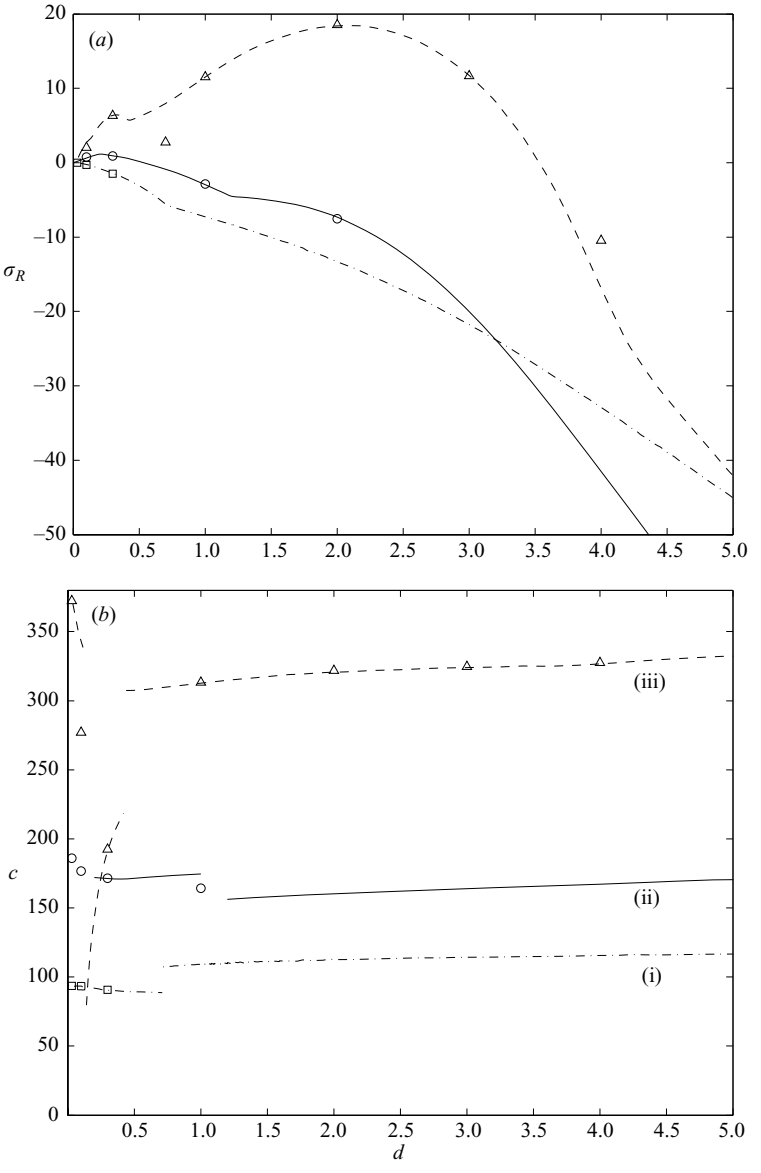

FIGURE 18. A comparison with Finlay's (1990) figures 7 and 8. (*a*) Growth rate and (*b*) wave speed against d (with $b=0$) for (i) $\Omega=8.00$, $\beta=3$ and $R=124.9$ (-.-); (ii) $\Omega=14.00$, $\beta=3$ and $R=260.8$ (–); and (iii) $\Omega=27.50$, $\beta=3$ and $R=532.1$ (- -). All our results were obtained for truncation level $L=15$, $N=7$. Finlay's (1990) corresponding results are given by (i) □, (ii) ○ and (iii) △.

to be slightly reduced, with in particular discrepancies existing between the figures for the growth rate at $d=0.7$, and also the wave speed at $d=0.1$. Regarding the latter, this discrepancy is perhaps related to the change in the most unstable eigenmode that occurs at around $d=0.14$, with a subsequent discontinuity in the wave speed about this point. Regarding the former discrepancy, we note, however, that despite the difference in results, the growth rate for case (*c*) has two maxima in agreement with Finlay's (1990) results, and we have confirmed Finlay's (1990) speculation that

the first maxima corresponds to a different eigenmode (the most unstable mode for $0.14 \leqslant d \leqslant 0.42$) to that of the second maxima. A visualization of an estimated form of the tertiary flow arising from this different mode is provided in figure 13(*b*), and is discussed in § 5.2.

We also performed a quantitative comparison with case II of the four cases for which numerical simulation results are presented by Yang & Kim (1991). Yang & Kim's (1991) table 1 states that the spanwise wavenumber of this nonlinear flow is the same as that found in the linear stage, which we understand to be the critical wavenumber when their rotation number $Rot^{YK} = 0.375$, for which we obtain $\beta_c = 2.7115$. Choosing the other parameters $\Omega = 42$ and $R = 88.39$ to agree with Yang & Kim's (1991) other dimensionless parameters for this case, we performed a secondary stability analysis of the flow. However, in contrast to the stability observed in Yang & Kim's (1991) figure 14, we found this flow to be unstable to disturbances of Eckhaus or small d type, similar to that shown (for different parameters) in figure 15. In fact, for this wavenumber, fixing $Rot^{YK} = 0.375$, we found that the flow first loses stability at $R^{YK} = 1.1R_c^{YK}$ where R^{YK} is Yang & Kim's (1991) Reynolds number, and R_c^{YK} denotes the linear critical value of R^{YK} for $Rot^{YK} = 0.375$. This is in contrast to the results of Yang & Kim's (1991) figure 14, which appear to show stability for $Rot^{YK} = 0.375$ and $\beta = 2.7115$ at $R^{YK} = 1.2R_c^{YK}$. However, we note that Yang & Kim (1991) stated that they chose the values of their parameters to concur with those of Alfredsson & Persson (1989). In this case their values of R^{YK} and Rot^{YK} correspond to those of the flow shown in figure 6(*e*) of Alfredsson & Persson's (1989) study. We have estimated the value of β from Alfredsson & Persson's (1989) photograph, and the value of β appears instead to be around 3.5, which is somewhat larger than the linear critical value, an issue which was commented on by Alfredsson & Persson (1989) in relation to their figure 6(*d*). With this observed value of β, together with $R = 88.33$ and $\Omega = 42$ chosen so that the other parameter values agree with those used by Alfredsson & Persson (1989) and Yang & Kim (1991) for this case, we performed another secondary stability analysis and we found the flow to be stable to all disturbances, in agreement with the behaviour observed in Alfredsson & Persson's (1989) photograph, and in agreement with the behaviour of the flow shown in Yang & Kim's (1991) figure 14. Such a stabilization gained by increasing the spanwise wavenumber may be attributed to moving inside the Eckhaus-stable closed region as may be seen with reference to figure 12.

7. Summary and conclusions

This study has considered the flow through a channel subject to system rotation about the spanwise axis. A global bifurcation approach has been used to compute finite-amplitude streamwise-independent nonlinear secondary flows. The stability of these flows to three-dimensional secondary disturbances has been analysed, and information about the bifurcating tertiary flow has been derived.

A rich structure of relationships between the secondary flows has been found to exist, which may be explained by the loss of stability of all of the flows to other elements of the solution set by a secondary Eckhaus disturbance mode, combined with the loss of stability of lower-order primary and secondary disturbance modes. The secondary flows exhibit a large area of near-zero absolute vorticity in the centre of the channel with increasing R, as has also been observed in previous turbulent experimental studies and numerical simulations.

A stability analysis of the secondary flows to three-dimensional disturbances has allowed us to confirm, clarify and add to the results of previous experimental and DNS-based studies. Overall, results from the present bifurcation approach find good qualitative and quantitative agreement with those of previous studies, with, in particular, excellent agreement with the experimental results of Alfredsson & Persson (1989). As R is increased from the critical value the secondary flow first loses stability to an Eckhaus disturbance (i.e. a streamwise-independent disturbance). With further increases in R the flow loses stability to other secondary disturbance modes including a mode with small but non-zero streamwise wavenumber, d, and fundamental spanwise wavenumber ($b=0$), which appears to correspond to the undulating wavy-vortex type II (WVF2) flows in Finlay's (1990) study. The strongest growing mode becomes one with $b=\beta/2$ and $d=O(1)$, and then a mode with $b=0$ and $d=O(1)$. The eigenvalues of the latter modes have non-zero imaginary parts, and these modes appear to correspond to the travelling-wave wavy vortex flow I (WVF1) of Finlay's (1990) study and also the twisting vortices observed in the experiments of Alfredsson & Persson (1989).

At values of R for which a stable steady streamwise-independent secondary flow solution still exists (i.e. values of R below the maximum value of R on the Eckhaus stability curve as shown in figure 12) we would expect the secondary flow to adjust its spanwise wavenumber to lie within the Eckhaus boundary. For small β this would thus involve an adjustment to higher values of β, or smaller wavelengths, which would be expected to be achieved by a splitting of some of the vortices. For large values of β a downward adjustment in the value of this parameter would be expected to be accompanied by a merging of some of the vortices. Although, as may be seen from figure 11, the secondary flow loses stability to three-dimensional modes immediately after losing stability to a two-dimensional (streamwise-independent) Eckhaus mode with increasing R, the Reynolds number must increase further before the three-dimensional modes become the strongest growing modes. Thus our results suggest that there may be an interval in R in which the growth of streamwise-independent disturbances dominates, while, however, no steady streamwise-independent secondary flow is stable. In this situation, the scenario described by the numerical simulations of Guo & Finlay (1991), in which there is a continual splitting and merging of the streamwise-orientated vortices, may occur. For reference we have included a curve in figure 12 showing where the secondary flow first loses stability to the subharmonic three-dimensional travelling-wave mode discussed in § 5.2. If the corresponding tertiary flow bifurcates supercritically the curve describes an existence curve for the corresponding tertiary flow.

Approximate visualizations of the tertiary flow by superimposing the secondary disturbance on the secondary flow suggest that these flows consist of a sequence of staggered (superharmonic bifurcation) or aligned (subharmonic bifurcation) vortices which lie either side of low-speed streamwise-orientated streaks in the streamwise velocity component. For the cases we have considered there is one such streak per spanwise wavelength of the flow for superharmonic bifurcations, and two such streaks for flows arising from subhamonic bifurcations. The present structures may be compared to breakdown and transitional structures observed in other non-rotating flows. In the later stages, both oblique and Tollmien–Schlichting (TS) transition routes, which may be studied in channel or boundary layer flows, lead to the formation of Λ-shaped vortices, either in staggered (oblique, H-type TS) or aligned (K-type TS) formation, as well as the streaky structures in streamwise velocity found in the present case. The present results do not exhibit any Λ-shaped structures, but an analysis of the

full nonlinear three-dimensional solutions for larger values of R is necessary to make a definitive comparison. However, we note that structures consisting of staggered vortices lying either side of low-speed streaks in streamwise velocity are a prevalent feature of the near-wall region of turbulent flows, as described by Jeong *et al.* (1997). Furthermore, upon introducing the wall unit length scale, ν/u_T, where

$$u_T = \sqrt{\nu |\mathrm{d}U^*/\mathrm{d}z^*|_{wall}},$$

it is found that the spanwise spacing of these low-speed streaks is consistently around 100 wall units, independent of the value of R. Waleffe (2003) recently computed exact coherent state solutions for plane Poiseuille and Couette flows under various combinations of slip/no-slip boundary conditions. In all cases, the solutions took the form of staggered quasi-streamwise vortices lying either side of wavy low-speed streaks, similar to the structures observed in the near-wall region of turbulent flows. Waleffe (2003) optimized the parameters of his exact coherent states so as to derive the lowest onset Reynolds numbers, and found the spanwise spacing of these states to be close to 100 wall units. For reference, the present flows depicted in figures 13(a), 13(b) and 13(c) have a spanwise spacing of 62, 74 and 104 respectively (where half the channel width corresponds to 25, 35 and 21 wall units respectively). Since these flows are some distance from the turbulent regime, and their disturbance wavelengths have not been optimized, a definitive comparison cannot be made, but the flows found in the present study originating from superharmonic bifurcations in particular are of a similar pattern to those found in near-wall regions of turbulent flow.

The authors would like to acknowledge the useful discussions held with M. Mastubara on this material.

REFERENCES

Alfredsson, P. H. & Persson, H. 1989 Instabilities in channel flow with system rotation. *J. Fluid Mech.* **202**, 543–557.

Bradshaw, P. 1969 The analogy between streamline curvature and buoyancy in turbulent shear flow. *J. Fluid Mech.* **36**, 177–191.

DiPrima, R. C. & Swinney, H. L. 1985 Instabilities and transition in flow between concentric rotating cylinders. In *Hydrodynamic Instabilities and the Transition to Turbulence* (ed. H. L. Swinney & J. P. Gollub) Topics in Applied Physics, vol. 45, pp. 139–180. Springer.

Drazin, P. G. & Reid, W. H. 1981 *Hydrodynamic Stability*. Cambridge University Press.

Eckhaus, W. 1965 *Studies in Nonlinear Stability Theory*. Springer.

Finlay, W. H. 1990 Transition to oscillatory motion in rotating channel flow. *J. Fluid Mech.* **215**, 209–227.

Finlay, W. H. 1992 Transition to turbulence in a rotating channel. *J. Fluid Mech.* **237**, 73–99.

Finlay, W. H., Keller, J. B. & Ferziger, J. H. 1988 Instability and transition in curved channel flow. *J. Fluid Mech.* **194**, 417–456.

Guo, Y. & Finlay, W. H. 1991 Splitting, merging and wavelength selection of vortices in curved and/or rotating channel flow due to Eckhaus instability. *J. Fluid Mech.* **228**, 661–691.

Hopfinger, E. J. & Linden, P. F. 1990 The effect of background rotation on fluid motions: a report on Euromech 245. *J. Fluid Mech.* **211**, 417–435.

Jeong, J., Hussain, F., Schoppa, W. & Kim, J. 1997 Coherent structures near the wall in a turbulent channel flow. *J. Fluid Mech.* **332**, 185–214.

Johnston, J. P., Halleen, R. M. & Lezius, D. K. 1972 Effects of spanwise rotation on the structure of two-dimensional fully developed turbulent channel flow. *J. Fluid Mech.* **56**, 533–557.

Kristoffersen, R. & Andersson, H. I. 1993 Direct simulations of low-Reynolds-number turbulent flow in a rotating channel. *J. Fluid Mech.* **256**, 163–197.

Lezius, D. K. & Johnstone, J. P. 1976 The structure and stability of turbulent boundary layers in rotating channel flow. *J. Fluid Mech.* **77**, 153– 175.

Matsubara, M. & Alfredsson, P. H. 1998 Secondary instability in rotating channel flow. *J. Fluid Mech.* **368**, 27–50.

Nagata, M. 1986 Bifurcations in Couette flow between almost corotating cylinders. *J. Fluid Mech.* **169**, 229–250.

Nagata, M. & Busse, F. 1983 Three-dimensional tertiary motion in a plane shear layer. *J. Fluid Mech.* **135**, 1–26.

Pedley, T. J. 1969 On the instability of viscous flow in a rapidly rotating pipe. *J. Fluid Mech.* **35**, 97–115.

Raszillier, H. & Durst, F. 1988 Forces of a fluid in rotating straight pipe. *Z. Angew. Math. Phys.* **39**, 397–403.

Tritton, D. J. 1992 Stabilization and destabilization of turbulent shear flow in a rotating fluid. *J. Fluid Mech.* **241**, 503–523.

Tritton, D. J. & Davies, P. A. 1985 In *Hydrodynamic Instabilities and the Transition to Turbulence* (ed. H. L. Swinney & J. P. Gollub), p. 229. Springer.

Waleffe, F. 1998 Three-dimensional coherent states in plane shear flows. *Phys. Rev. Lett.* **81**, 4140–4143.

Waleffe, F. 2003 Homotopy of exact coherent structures in plane shear flows. *Phys. Fluids* **15**, 1517–1534.

Wall, D. P. & Nagata, M. 2000 Nonlinear equilibrium solutions for the channel flow of fluid with temperature-dependent viscosity. *J. Fluid Mech.* **406**, 1–26.

Yang, K. S. & Kim, J. 1991 Numerical investigation of instability and transition in rotating plane Poiseuille flow. *Phys. Fluids* A 3, 633–641.